MDPI

Article

Investigation of the Effectiveness of Silicon Nitride as a Reinforcement Agent for Polyethylene Terephthalate Glycol in Material Extrusion 3D Printing

Nikolaos Michailidis [1,2], Markos Petousis [3], Vassilis Saltas [4], Vassilis Papadakis [5,6], Mariza Spiridaki [3], Nikolaos Mountakis [3], Apostolos Argyros [1,2], John Valsamos [3], Nektarios K. Nasikas [7] and Nectarios Vidakis [3,*]

1 Physical Metallurgy Laboratory, Mechanical Engineering Department, School of Engineering, Aristotle University of Thessaloniki, 54124 Thessaloniki, Greece; nmichail@auth.gr (N.M.); aargyros@auth.gr (A.A.)
2 Centre for Research & Development of Advanced Materials (CERDAM), Centre for Interdisciplinary Research and Innovation, Balkan Centre, Building B', 10th Km Thessaloniki-Thermi Road, 57001 Thessaloniki, Greece
3 Department of Mechanical Engineering, Hellenic Mediterranean University, 71410 Heraklion, Greece; markospetousis@hmu.gr (M.P.); mspyridaki@hmu.gr (M.S.); mountakis@hmu.gr (N.M.); valsamos@hmu.gr (J.V.)
4 Department of Electronic Engineering, Hellenic Mediterranean University, 73133 Chania, Greece; saltas@hmu.gr
5 Institute of Electronic Structure and Laser of the Foundation for Research and Technology-Hellas (IESL-FORTH)—Hellas, N. Plastira 100m, 70013 Heraklion, Greece; v.papadakis@uniwa.gr
6 Department of Industrial Design and Production Engineering, University of West Attica, 12243 Athens, Greece
7 Division of Mathematics and Engineering Sciences, Department of Military Sciences, Hellenic Army Academy, 16673 Vari, Greece; nasikas@sse.gr
* Correspondence: vidakis@hmu.gr; Tel.: +30-2810379227

Abstract: Polyethylene terephthalate glycol (PETG) and silicon nitride (Si_3N_4) were combined to create five composite materials with Si_3N_4 loadings ranging from 2.0 wt.% to 10.0 wt.%. The goal was to improve the mechanical properties of PETG in material extrusion (MEX) additive manufacturing (AM) and assess the effectiveness of Si_3N_4 as a reinforcing agent for this particular polymer. The process began with the production of filaments, which were subsequently fed into a 3D printer to create various specimens. The specimens were manufactured according to international standards to ensure their suitability for various tests. The thermal, rheological, mechanical, electrical, and morphological properties of the prepared samples were evaluated. The mechanical performance investigations performed included tensile, flexural, Charpy impact, and microhardness tests. Scanning electron microscopy and energy-dispersive X-ray spectroscopy mapping were performed to investigate the structures and morphologies of the samples, respectively. Among all the composites tested, the PETG/6.0 wt.% Si_3N_4 showed the greatest improvement in mechanical properties (with a 24.5% increase in tensile strength compared to unfilled PETG polymer), indicating its potential for use in MEX 3D printing when enhanced mechanical performance is required from the PETG polymer.

1. Introduction

Additive manufacturing (AM) technology has been the subject of intense research and development for over 30 years, resulting in constant progress and innovative techniques that constitute a true revolution in manufacturing. AM processes include most notably stereolithography (SLA) [1], fused deposition modeling (FDM) [2], three-dimensional printing (3DP) [3], selective laser sintering (SLS) [4], laminated objective manufacturing (LOM) [5], and laser metal deposition (LMD) [6]. AM provides the opportunity to create

parts with complex geometries in a shorter period of time and at a significantly lower cost [7] than traditional manufacturing techniques [8]. AM has important and innovative applications in a variety of fields, such as engineering [9], aerospace [10–15], the automotive industry [11,12,16,17], energy [18], the use of ceramic materials [19], electronics [20,21], defense [22,23], and medicine [24–29].

Fused filament fabrication (FFF) or material extrusion (MEX) can easily be utilized for the processing of polymers and reinforced polymers because it is a simple procedure that involves feeding an extrusion-suitable thermoplastic filament into a nozzle and fabricating the desired 3D sample [30,31]. It should be mentioned that some settings must be properly and carefully set during each FFF procedure because they can influence the mechanical performance of the 3D-printed sample [32,33]. Those could be, among others, the printing speed, the layer thickness, the temperature of the nozzle, the bed, and the chamber, etc. [34,35].

Polyethylene terephthalate glycol (PETG) is the most common thermoplastic polymer resin among polyesters. It is a modified polyethylene terephthalate (PET) polymer filled with glycol that provides better processability in the FFF technique [36,37]. It possesses some advanced properties compared to PET, such as chemical alkali resistance, high shrinkage, transparency, gloss, low haze, good printability [38], and processability, along with the ability to be easily mixed with blends [39]. It can be useful in applications that require more enhanced mechanical properties than PET; moreover, its 3D-printing FFF process is easy to use, and it can be utilized for food packaging [38], engineering [40], and medical applications [41], among others.

Many industries tend to choose ceramics for specific applications owing to their advanced properties [42] such as high hardness and high melting temperature (Tm). Such quantities are utilized in applications featuring high loads, such as in cutting tools [43,44]. Silicon nitride (Si_3N_4) is a ceramic material that exhibits extraordinary properties, such as high durability, potency, crack-withstanding ability, and resistance to sudden temperature changes [45–47]. Therefore, such ceramics and analogous materials are suitable for specific applications that require optimal operation under harsh working conditions, such as bearings [48], hard coatings, cutting tools [49], spark plugs [50,51], and engine parts that operate at high temperatures [52]. According to many studies, the presence of nitride nanoparticles can be beneficial to the characteristics and behavior of polymer nanocomposites with regard to their thermomechanical properties [47,53,54]. In addition to its excellent mechanical properties as a ceramic material, Si_3N_4 is considered a bioceramic that can be useful for medical or healthcare applications. It is a subject of interest in the field of biomedicine because of its biocompatibility and superior chemical, physical, and mechanical properties, which are necessary for applications such as implants [55,56] and scaffolds [57,58]. Si_3N_4 ceramics are also characterized by their bacteriostatic properties, which can be useful in a variety of biomedical applications [45,46]. Recently, they have been used in biomedical applications such as in 3D printing using material extrusion (MEX) [59,60] and vat photopolymerization (VPP) [61,62] methods.

In this research endeavor, various composites were developed by blending PETG as the matrix material with Si_3N_4 ceramic as the filler, with the aim of evaluating their performance in a range of tests. This study examined the impact of Si_3N_4 nanoparticles as reinforcing agents for PETG thermoplastic. The objective was to enhance the mechanical properties of PETG thermoplastic in MEX 3D printing, with an emphasis on developing a process that could be scaled up for industrial production. This enhancement is intended to improve the durability of components, particularly in applications where PETG thermoplastic is the preferred polymer, thus potentially expanding its range of use. It is worth noting that this investigation into PETG/Si_3N_4 nanocomposites, especially in terms of their mechanical properties, is novel in the literature, particularly within the realm of additive manufacturing (AM) or MEX 3D printing technologies.

In this study, PETG was used in conjunction with Si_3N_4 to create composites with five filler percentages (2.0, 4.0, 6.0, 8.0, and 10.0 wt.%). The corresponding mixtures were created

and used to fabricate filaments via material extrusion (MEX). The produced filaments were later fed into a three-dimensional printer (3D-P) to fabricate the desired specimens in accordance with the respective international standards, for which the specimens subsequently underwent a variety of tests. The same settings were applied for the fabrication of all the samples so that the results would be comparable. The samples were subjected to a series of mechanical tests, including tensile, flexural, impact, and microhardness tests. Thermogravimetric analysis (TGA), differential scanning calorimetry (DSC), and Raman spectroscopy were used to determine the thermal properties of the composites. Their electrical/dielectric properties over a broad frequency range were examined, and scanning electron microscopy (SEM) and energy-dispersive X-ray spectroscopy (EDS) were employed to reveal the structural characteristics and chemical compositions of the samples. Micro-CT (μ-CT) was used to determine the dimensional accuracy and internal structure of the fabricated samples. A significant enhancement in the mechanical properties was exhibited by the 6.0 wt.% composite made of Si_3N_4, which led to this specific filler percentage composite being considered suitable for providing the nanocomposites with reinforced mechanical properties. However, the electrical/dielectric response of PETG/Si_3N_4 composites is mainly dependent on the electrical behavior of the polymer matrix. This study aims to achieve the following:

- Examine the ability of Si_3N_4 to enhance the mechanical properties and reinforce the performance of the PETG polymer.
- Determine the contribution of Si_3N_4 to the electrical/dielectric properties of the PETG polymer.
- Investigate and provide evidence for the suitability of PETG/Si_3N_4 composites for use as 3D printable materials for the fabrication of various parts that can serve a constantly increasing variety of applications in demanding and extreme environments.

2. Materials and Methods

The present work involved a series of steps, summarized in Figure 1, regarding the preparation of the raw materials, filaments, and specimens as well as the tests conducted on them. Figure 1A,B display the raw materials prepared and dried in an oven to remove any absorbed moisture. As shown in Figure 1C,D, the filaments were extruded and allowed to dry in an oven, while Figure 1E,F show their quality inspection and mechanical testing. Figure 1G,H show the material extrusion 3D-P of the corresponding specimens and their quality control. Figure 1I,J concern the mechanical testing and evaluation of the specimens, while their rheological and morphological characteristics are shown in Figure 1K,L.

2.1. Materials

Polyethylene Terephthalate Glycol (PETG) was supplied by Felfil Srl (Torino, Italy) in pellet form. Nanographi (Ankara, Turkey) was used as the source of silicon nitride (Si_3N_4) nanoparticles (Ankara, Turkey).

2.2. Preparation of the PETG/Si_3N_4 Filament and 3D Printing

Preparation of PETG/x wt.% Si_3N_4 filaments began by measuring the correct quantities of both materials and then using them to synthesize the desired compounds. As to the definition of the filler percentage limit, it was set according to the results of preliminary tests conducted on the samples, while gradually increasing the filler quantity. Increasing the amount of additive was discontinued when the performance of the samples ceased to provide useful results and information. Apart from the pure PETG quantity, which was prepared, five different mixtures of PETG/x wt.% Si_3N_4 were also compounded, namely, PETG/2.0 wt.% Si_3N_4, PETG/4.0 wt.% Si_3N_4, PETG/6.0 wt.% Si_3N_4, PETG/8.0 wt.% Si_3N_4, and PETG/10.0 wt.% Si_3N_4. After being left in the oven overnight at 80 °C to dry, the filaments were fed onto a 3D Evo Composer single-screw 450 extruder supplied by 3devo (3devo B. V., Utrecht, The Netherlands). It should be noted that the diameter of the filaments was monitored during extrusion using a filament diameter sensor with the ability to make micro-adjustments, if needed, to the extrusion speed. The available literature provided

this study with the necessary information about the extrusion parameters. The diameter for all filaments remained almost steady at a range between 1.65 mm and 1.85 mm, which is considered suitable for the 3D-P of the specimens. The filaments, which were dried overnight at 80 °C, were subsequently supplied to an FFF Intamsys Funmat HT 3D printer purchased from Intamsys Technology Co., Ltd. (Shanghai, China) for the production of 3D-P specimens. They were designed using 3D Autodesk® Fusion 360™ software (Autodesk®, Inc, San Francisco, CA, USA, https://www.autodesk.com/campaigns/education/fusion-360, accessed on 20 November 2023) and exported into Standard Tesselation Language (STL) format files.
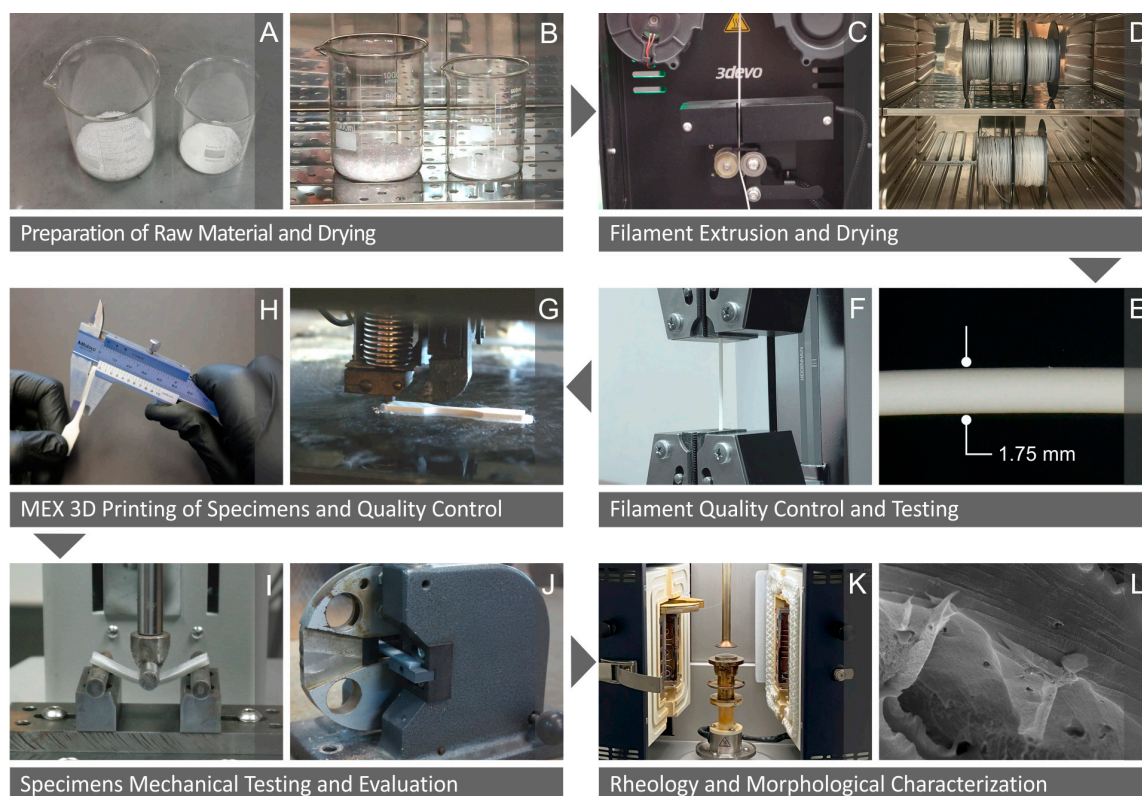

Figure 1. The steps followed in the present study include (**A**) the preparation of the unprocessed materials and (**B**) their drying; (**C**) the production of the filaments through extrusion and (**D**) their subsequent drying; (**E**) inspection of quality and (**F**) mechanical testing; the (**G**) material extrusion of the three-dimensional specimens and (**H**) the inspection of their quality; (**I,J**) examination and evaluation of mechanical properties; and (**K**) rheological and (**L**) morphological investigation.

2.3. SEM of Si_3N_4 and EDS Analysis

Scanning electron microscopy (SEM) analysis was conducted by capturing fracture and side surface images of the specimens using an electron Jeol JSM-IT700HR (Jeol Ltd., Tokyo, Japan) field-emission scanning electron microscope. The chemical elements of the samples were detected via EDS analysis using the same device employed for SEM. The chemical composition of Si_3N_4 was investigated using the same procedure. The scanning electron microscope was operated in high-vacuum mode with a 5 kV acceleration voltage, and the samples were gold-sputtered during the SEM and EDS analyses.

In Figure 2A, an SEM image of Si_3N_4 at 10,000× magnification is presented, and the highlighted square area is shown in Figure 2B at 20,000× magnification. The highlighted square area in Figure 2B is magnified 50,000× (Figure 2C). The EDS mapping results for Si_3N_4 are shown in Figure 2D, and Figure 2C shows the chemical composition analysis derived from the EDS. As can be observed, high levels of Si were detected, which was an expected phenomenon.
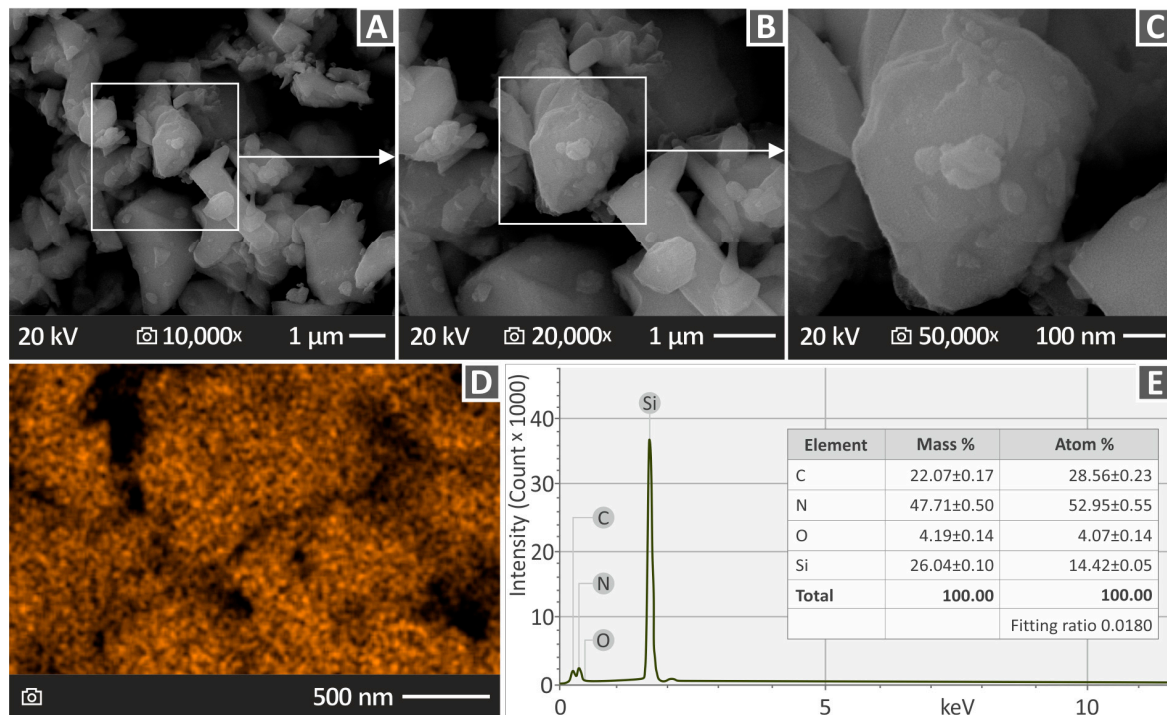
Figure 2. Analyzation of the unprocessed material of Si_3N_4 through (**A**) SEM pictures magnifying specific areas of the material at 10,000×, (**B**) 20,000×, and (**C**) 50,000× as well as (**D**) an EDS mapping image and (**E**) a chemical composition analysis via EDS.

2.4. Mechanical Tests

The various mechanical tests conducted on the specimens included tensile, flexural, Charpy impact, and microhardness (MH) tests. Several 3.2 mm thick V-type tensile specimens were created and tested according to the American Society for Testing and Materials (ASTM) standard D638-02a [63]. The specimens were placed between the standardized grips of an Imada MX2 (Imada Inc., Northbrook, IL, USA) tension/flexure test device in tensile mode for the tensile tests. The same machine but in flexural mode was used for flexural 3-point bending tests based on ASTM D790-10 [64] (3-point bending test with a 52.0 mm support span). ASTM D6110-04 [65] was used for impact testing, which was conducted using a Charpy impact apparatus (Terco MT 220, Terco, Sweden). ASTM E384-17 [66] was used for M–H measurements, and a Vickers apparatus, Innova Test 300 (Europe BV, Maastricht, The Netherlands), was used on specimens whose surfaces were preliminarily fully polished under a force of 100 gF and for an indentation duration of 10 s.

On the left side of Figure 3, the set 3D-P parameters are presented, along with some samples from the actual 3D-printed tensile, flexural, and impact specimens. The nozzle temperature was set to 240 °C, the bed temperature was 80 °C, the thickness of the layers was 0.2 mm, and the travel speed was 40 mm/s. On the right side of Figure 3, the initially designed models of the tensile, flexural, and impact specimens are presented along with their dimensions and related ASTM standards.

2.5. Raman Spectroscopy

A confocal LabRAM HR Raman spectrometer (HORIBA Scientific, Kyoto, Japan) was employed to obtain Raman Spectroscopy measurements under laboratory conditions. A 532 nm laser line was used for Raman signal excitation with a power of 90 mW. To help control the laser power applied to the sample, a 5% neutral-density filter was placed in the optical path of the laser beam. The laser was focused on the sample with a 50× microscope Olympus objective lens (LMPlanFL N) with a Numerical Aperture (NA) and a 10.6 mm working distance. The Raman signal was collected using the same objective lens and visualization of the sample area. The acquisition settings used in this study were as follows:

- Measurement spectral sensitivity range (50 up to 3900 cm^{-1});
- Spectral resolution (2 cm^{-1});
- Spectrometer grating (600 grooves/mm);
- Exposure time at each measurement point (10 s);
- Measurement accumulations per point (5);
- Measurement point dimensions (1.7 μm laterally and 2 μm axially).

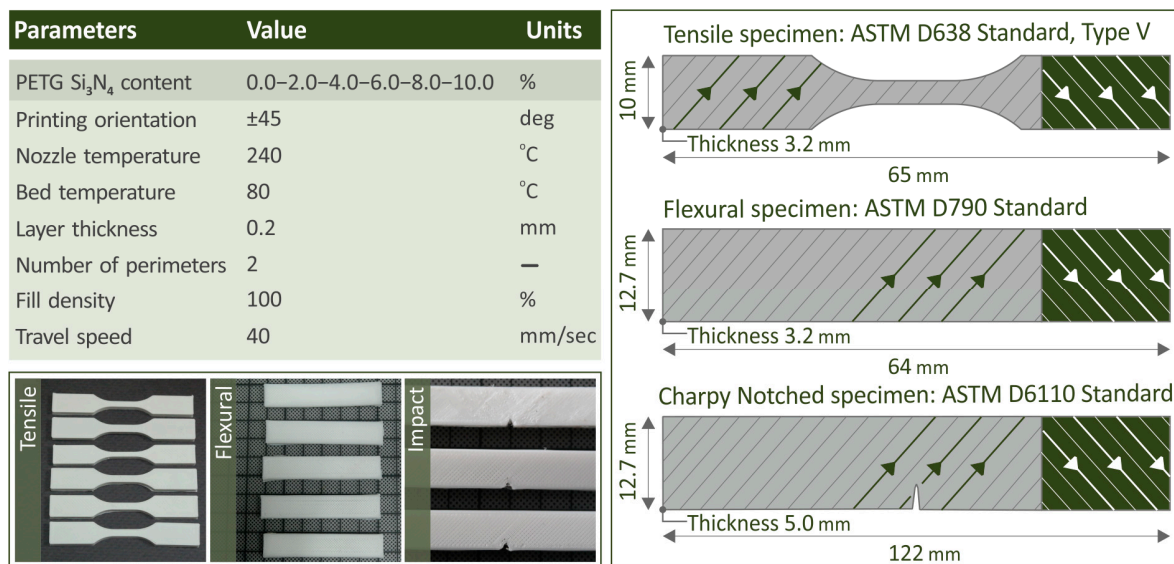| Parameters	Value	Units
PETG Si$_3$N$_4$ content	0.0–2.0–4.0–6.0–8.0–10.0	%
Printing orientation	±45	deg
Nozzle temperature	240	°C
Bed temperature	80	°C
Layer thickness	0.2	mm
Number of perimeters	2	—
Fill density	100	%
Travel speed	40	mm/sec

Figure 3. (**Top left area of the figure**) A data board including the printing parameters of the specimens, (**bottom left area of the figure**) the actual 3D-P specimens, and (**right area of the figure**) the initially designed models of the specimens. The arrows on the specimens on the right side indicate the built pattern orientation, which is changing by 90 degrees (±45 degrees) between the successive layers.

The laser power resulting from the surface of the sample was 2 mW.

Following each measurement, any possible discoloration or degradation caused by laser irradiation was detected by visually inspecting the irradiated areas. No such events were detected in the Raman spectroscopy measurements, as described above, ensuring that the parameters for obtaining various Raman spectra were optimal.

2.6. Thermogravimetric and Differential Scanning Calorimetry Analyses

The thermal behaviors of the samples derived from the PETG/x wt.% Si$_3$N$_4$ composites and the pure PETG were examined by means of thermogravimetric analysis (TGA) and differential scanning calorimetry (DSC). The apparatus used was a Diamond Perkin Elmer (Waltham, MA, USA) with a 40–550 °C temperature cycle at an increase rate of 10 °C/min. A Discovery Series DSC-25 DSC calorimeter (TA Instruments, New Castle, DE, USA) was used to obtain DSC measurements, along with an RSC-90 Refrigerated Cooling System. The TGA and DSC analyses were conducted in an inert environment in the presence of high-purity N$_2$ (nitrogen gas).

2.7. Investigation of the Rheometric Behavior

A DHR-20 Discovery Hybrid Rotational Rheometer (TA Instruments, DE, USA) was used to record rheological measurements, according to ASTM D1238-13 [67], for the melt flow rate (MFR). An Environmental Test Chamber with a parallel-plate setup was used for temperature regulation, and the duration of the acquisition was set to 10 s at every measurement point, with the aim of preventing excessive heating and decomposition. Melt flow rate (MFR) and rotational rheometric tests were used to assess the flow rates of the materials at certain temperatures and previously determined pressures.

2.8. Broadband Dielectric Spectroscopy (BDS) Examination

Dielectric spectroscopy measurements of PETG/x wt.% Si_3N_4 composites were performed using an Alpha-ANB high-resolution dielectric analyzer combined with a ZGS Alpha Active sample holder and BDS 1100 module (Novocontrol Technologies GmbH & Co., Montabaur, Germany). Measurements were performed in the frequency range of 10^{-2} Hz–4 MHz at room temperature. Disk-shaped specimens with a diameter of 40 mm and a thickness of 4 mm were prepared via thermal pressing to form the dielectric material of the sandwich-structured capacitor in a two-electrode configuration. A conductive paste was applied to both sides of the specimens to ensure proper electrical contact with the gold-plated electrodes of the sample holder. The applied ac voltage was set to $V_{rms} = 1$ V. WinDeta software, developed by Novocontrol Technologies (Novocontrol Technologies GmbH & Co., Montabaur, Germany, https://www.novocontrol.de/php/windeta.php, accessed on 20 December 2023), was used to control the experiments and acquire data.

The dielectric results are presented as the complex dielectric permittivity $\varepsilon^*(\omega)$, dissipation factor $\tan(\delta)$, and complex AC conductivity $\sigma^*(\omega)$ according to the following equations:

$$\varepsilon^*(\omega) = \varepsilon' - i\varepsilon'' = \frac{C(\omega)}{C_o} - i\frac{1}{\omega \cdot C_o \cdot R(\omega)} \tag{1}$$

$$\tan(\delta) = \frac{\varepsilon''}{\varepsilon'} \tag{2}$$

and

$$\sigma^*(\omega) = \sigma' - i\sigma'' = i\omega\varepsilon_o(\varepsilon^*(\omega) - 1) = \omega\varepsilon_o\varepsilon'' - i\omega\varepsilon_o(\varepsilon' - 1) \tag{3}$$

where $R(\omega)$ and $C(\omega)$ are the resistance and capacitance of the equivalent circuit in parallel connection measured using the dielectric analyzer, $C_o = \varepsilon_o \cdot \pi \cdot r^2/d$ is the capacitance of the empty cylindrical sample cell with radius r and distance d between the electrodes, $\omega = 2\pi f$ is the angular frequency, and ε_o is the permittivity of the vacuum. The real part of the dielectric permittivity (ε') measures the energy storage under the effect of an applied electric field, whereas the dissipation factor $\tan(\delta)$ ε'' is related to the energy loss within the material.

2.9. Micro-Computed Tomography

The porosity and dimensional deviation of the manufactured 3D-P specimens were examined using micro-CT (μ-CT). A CT scanner, namely, a Tomoscope HV Compact 225 kV Micro Focus (Werth Messtechnik GmbH, Giessen, Germany), with a 1024 × 1024-pixel sensor was employed along with VG Studio MAX 2.2 software (Volume Graphics GmbH, Heidelberg, Germany) for data processing. Through these examinations, the effects of additives on the 3D-P structure were evaluated. A 75 L setup (72.58 μm resolution on the *X*-axis and 72.65 μm resolution on the *Y*-axis) was used to examine dimensional accuracy. A 16 L setup (15.46 μm resolution on the *X*-axis and 15.49 μm resolution on the *Y*-axis) was used to examine porosity. A total of 1600 sections per revolution were acquired for both cases.

3. Results

3.1. Raman Results for PETG/x wt.% Si_3N_4 Composites

Figure 4a shows the Raman spectra of the pure PETG and PETG/x wt.% Si_3N_4 composites, while in Figure 4b, the results obtained by subtracting pure PETG from all the spectra of Figure 4a are presented.

In Table 1, the related Raman peaks from the pure PETG sample are presented as extracted from the literature, along with their references in brackets, indicating the work(s) from whence the data originated.
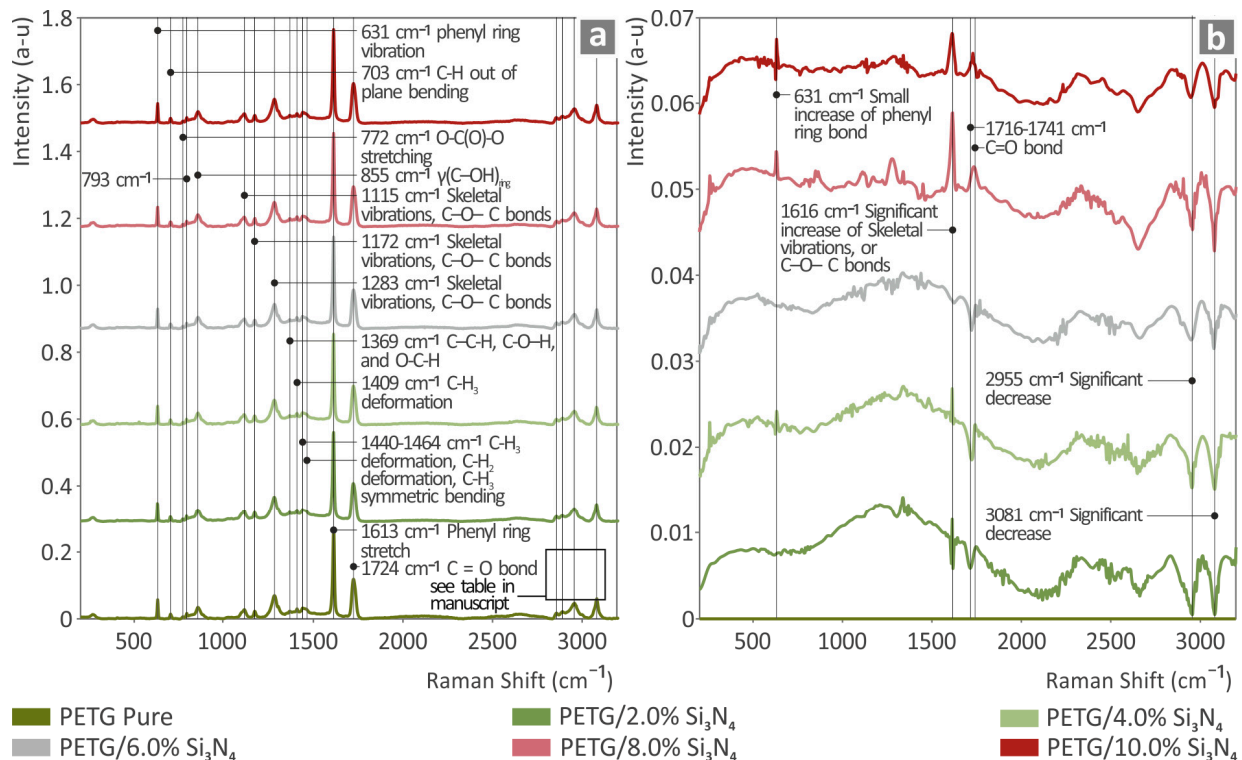
Figure 4. Representation of (**a**) the Raman graphs of the neat PETG and the PETG/x wt.% Si$_3$N$_4$ (x = 2.0, 4.0, 6.0, 8.0, and 10.0 wt.%) samples, accompanied by the (**b**) graphs created by the subtraction of the pure PETG spectral signature.

Table 1. Significant Raman peaks and their related assignments from pure PETG.

Wavenumber (cm^{-1})	Intensity	Raman Peak Assignment
631	Strong	phenyl ring vibration [68,69]
703	Medium	C-H out-of-plane bending [68]
772	Small	O-C(O)-O stretching [69]
793	Medium	
855	Strong	γ(C–OH)$_{ring}$ [70,71]
1115	Strong	Skeletal vibrations, C–O–C bonds [72]
1172	Strong	Skeletal vibrations, C–O–C bonds [68,72]
1283	Strong	Skeletal vibrations, C–O–C bonds [68,72]
1369	Small	C–C–H, C–O–H, and O–C–H [72]
1409	Medium	C-H$_3$ deformation [73]
1440–1464	Medium	C-H$_3$ deformation [68,73]; C-H$_2$ deformation [72]; C-H$_3$ symmetric bending [69,73,74]
1613	Very Strong	Phenyl ring stretch [69]
1724	Very Strong	C=O bond [75]
2857	Medium	C-H$_2$ symmetric stretching [72]
2890	Medium	CH$_2$ symmetric stretching [72,76]
2955	Strong	CH$_2$ asymmetric stretching [72]
3081	Strong	C-H stretching [73]

As shown in Figure 4a, as the concentration of Si$_3$N$_4$ increased in the PETG composite, the related Raman lines of the pure PETG differentiated in intensity. Furthermore, broad photoluminescence appeared to increase as the Si$_3$N$_4$ concentration increased in the spectral region from 800 to 1800 cm^{-1}.

The addition of Si_3N_4 to PETG resulted in an increase in the intensity of the phenyl ring bond at 631 cm^{-1} and a gradual increase in the intensity of the C–O–C bonds at 1616 cm^{-1}. A significant decrease in intensity was also observed in the Raman peaks at 2955 cm^{-1} and 3081 cm^{-1}, corresponding to the C-H2 and C-H bond stretching modes, respectively. A somewhat inconsistent behavior was observed in the 1716–1741 cm^{-1} spectral range, where C=O bonds were present. In low-concentration Si_3N_4 composites with compositions bearing 2 wt.%, 4 wt.%, and 6 wt.% Si_3N_4, respectively, an intensity decrease was found. In contrast, for the 8 wt.% and 10 wt.% Si_3N_4 composites, the intensity increased. This information is presented in Table 2.

Table 2. Significant Raman peak differences between the PETG/Si_3N_4 samples and PETG/pure.

631	Peak rise	Small increase in phenyl ring bond
1616	Gradual increase	Significant increase in skeletal vibrations or C–O–C bonds
1716–1741	Inconsistent behavior	C=O bond [75]
2955	Peak drop	Significant decrease
3081	Peak drop	Significant decrease

3.2. Thermogravimetric and Differential Scanning Calorimetry Analysis

Figure 5a shows the weights of the temperature curves of PETG/2.0% Si_3N_4, PETG/4.0% Si_3N_4, PETG/6.0% Si_3N_4, PETG/8.0% Si_3N_4, PETG/10.0% Si_3N_4, and pure PETG as well as an inset graph of their weight loss values depending on the filler percentage. Figure 5b shows the heat flow as temperature curves for the PETG/x wt.% Si_3N_4 with x = 2.0, 4.0, 6.0, 8.0, and 10.0 wt.%, respectively, and pure PETG, along with the glass transition (Tg) temperatures for each filler percentage included in the inserted graph.
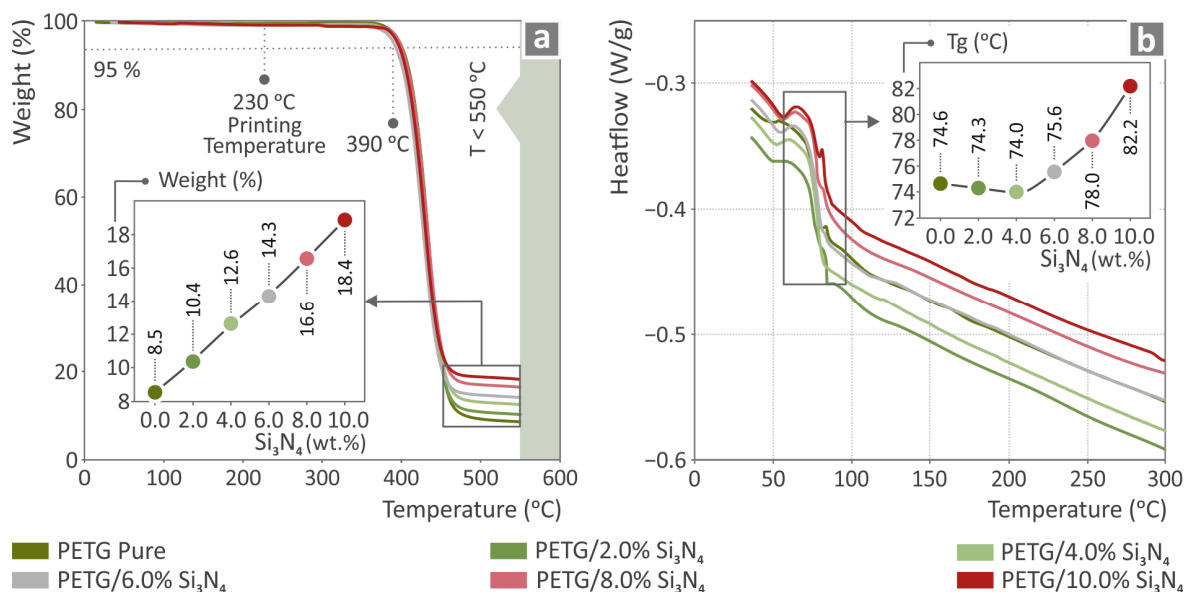

Figure 5. Pure PETG and PETG/x wt.% Si_3N_4 (x = 2.0, 4.0, 6.0, 8.0, and 10.0 wt.%) analyzed (**a**) thermogravimetrically and through (**b**) differential scanning calorimetry.

3.3. Viscosity and MFR Analysis

The solid lines in Figure 6a represent the viscosity values of all the PETG/x wt.% Si_3N_4 composites and pure PETG, whereas the dotted lines indicate their stress values at 240 °C. It can be observed that as the filler percentage increased, the viscosity increased, whereas the stress was not significantly influenced. Moreover, the viscosity decreased as the stress increased. Figure 6b shows the MFR values with respect to the Si_3N_4 filler percentage for

the PETG/x wt.% Si_3N_4, x = 2.0, 4.0, 6.0, 8.0, and 10.0 wt.% composites and pure PETG at 250 °C, at which point it is evident that PETG/4.0% Si_3N_4 has the highest value.
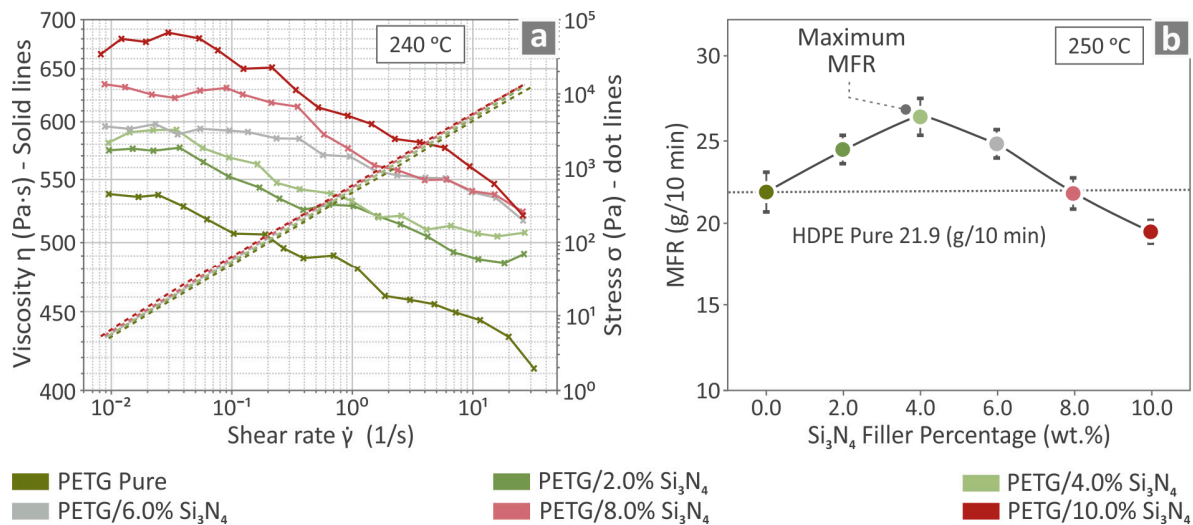

Figure 6. Pure PETG and PETG/x wt.% Si_3N_4 (x = 2.0, 4.0, 6.0, 8.0, and 10.0 wt.%) analyzed for (**a**) their viscosity properties at 240 °C and (**b**) their rates of melting flow at 250 °C.

3.4. Monitoring of the Filament

The extrusions of the pure PETG and PETG/4.0 wt.% Si_3N_4 filaments were monitored in order to observe the quality and diameter of the extruded material, and the results are shown in Figures 7a and 7b, respectively, along with pictures of the materials. The filaments seem to have a high-quality surface, without defects, while also being able to maintain an almost steady diameter ranging between 1.65 mm and 1.85 mm. The ultimate strength and Young's modulus results corresponding to those of the PETG/x wt.% Si_3N_4 with x = 2.0, 4.0, 6.0, 8.0, and 10.0 wt.%, respectively, and pure PETG filaments are contained in Figures 7c and 7d respectively. The recorded values for PETG/6.0 wt.% Si_3N_4 were higher than those of the other composites with other filler percentages, revealing an 18.8% increase with respect to pure PETG in the case of ultimate strength and a 19.0% increase with respect to pure PETG in the case of Young's modulus.

3.5. Mechanical Tests

The prepared composites, namely, PETG/2.0 wt.% Si_3N_4, PETG/4.0 wt.% Si_3N_4, PETG/6.0 wt.% Si_3N_4, PETG/8.0 wt.% Si_3N_4, PETG/10.0 wt.% Si_3N_4, and pure PETG, were all tested for their tensile mechanical responses, and the results are presented in Figure 8. In Figure 8a, the tensile stress curves are shown for all the prepared composites, and in Figure 8b,c, the ultimate strength and Young's modulus values are presented. The PETG/6.0 wt.% Si_3N_4 composite exhibited the highest values, with a 24.5% ultimate strength and an 18.3% Young's modulus, higher than those of pure PETG.

All the prepared composites, namely, PETG/2.0 wt.% Si_3N_4, PETG/4.0 wt.% Si_3N_4, PETG/6.0 wt.% Si_3N_4, PETG/8.0 wt.% Si_3N_4, PETG/10.0 wt.% Si_3N_4, and pure PETG were also tested for their flexural mechanical responses, and the results are shown in Figure 9. Figure 9a shows the flexural stress curves, while Figures 9b and 9c present the bending strength and bending modulus values, respectively. PETG/6.0 wt.% Si_3N_4 showed the highest values, with a 16.6% bending strength and a 16.8% bending modulus, constituting higher values than those of neat PETG.
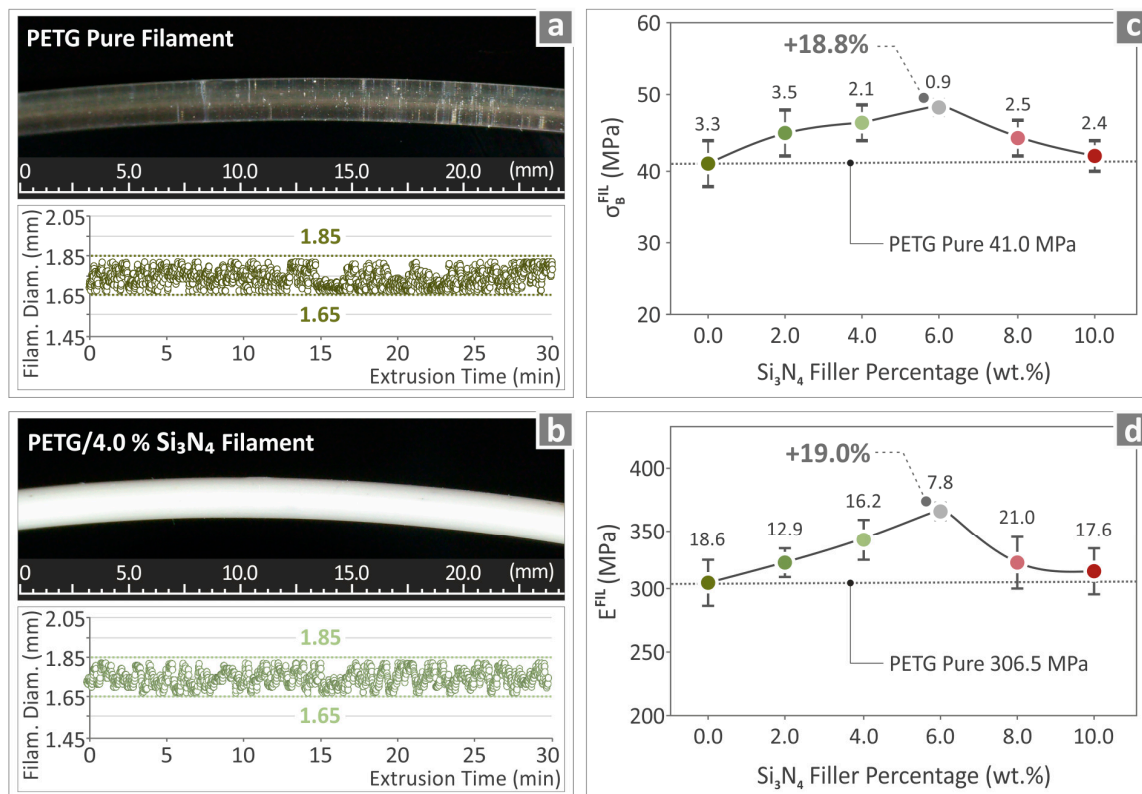
Figure 7. (**a**) Image of pure PETG filament and recorded measurements of its diameter, (**b**) image of PETG/4.0 wt.% Si_3N_4 filament and the recorded measurements of its diameter, and (**c**) tensile strength and (**d**) tensile modulus of elasticity of the filaments for all the employed filler percentages.
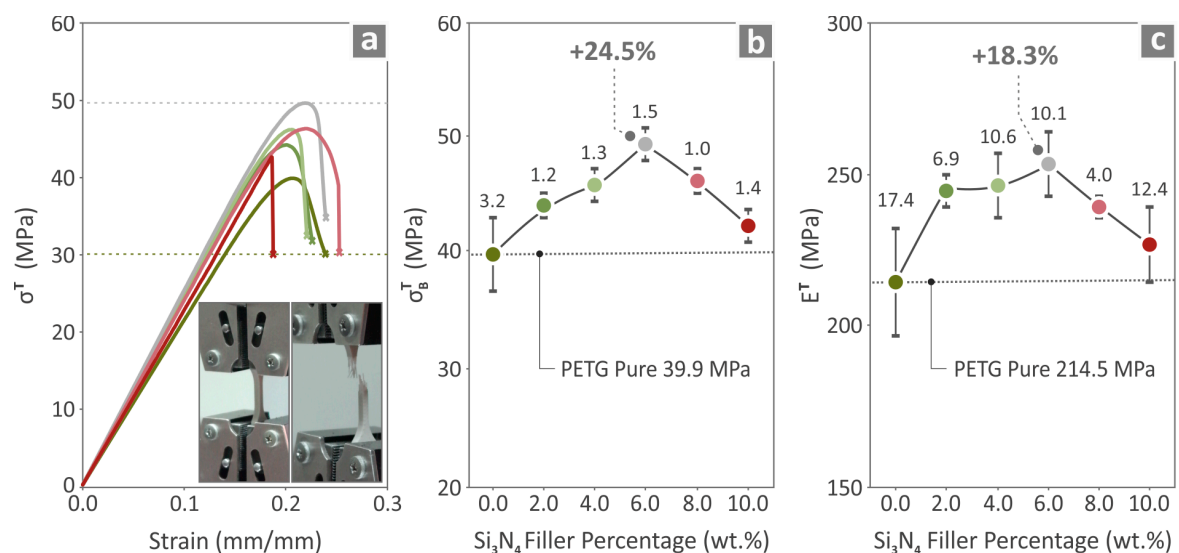

Figure 8. Results for pure PETG and PETG/x wt.% Si_3N_4 (x = 2.0, 4.0, 6.0, 8.0, and 10.0 wt.%) specimens about (**a**) tensile stress-to-strain graphs, (**b**) ultimate strength, and (**c**) Young's modulus.
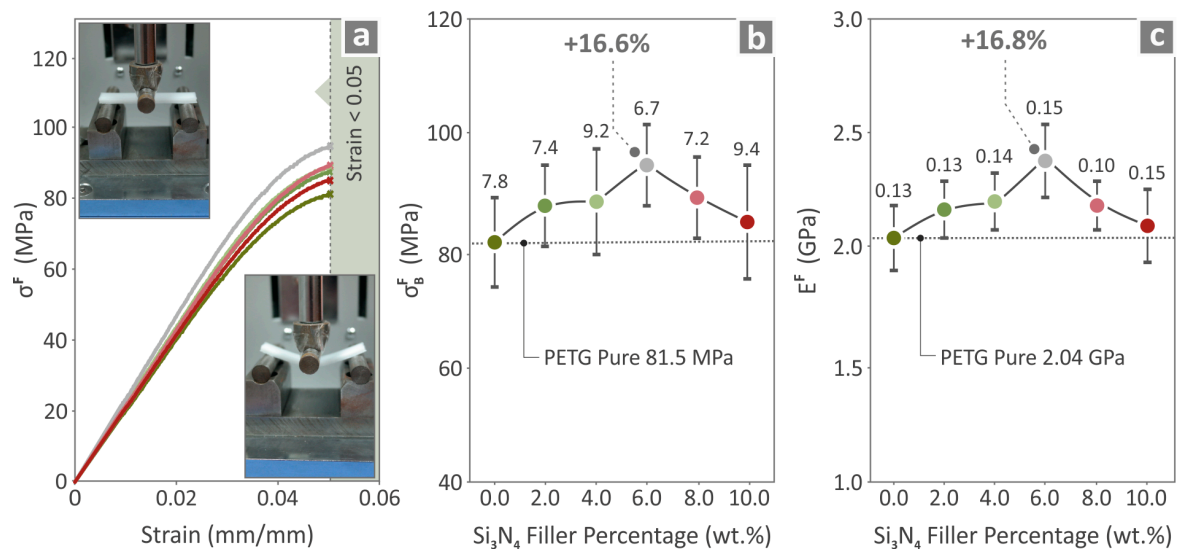
Figure 9. Results for pure PETG and PETG/x wt.% Si_3N_4 (x = 2.0, 4.0, 6.0, 8.0, and 10.0 wt.%) specimens about (**a**) flexural stress-to-strain graphs, (**b**) bending strength, and (**c**) bending modulus.

The results for the pure PETG, PETG/2.0 wt.% Si_3N_4, PETG/4.0 wt.% Si_3N_4, PETG/6.0 wt.% Si_3N_4, PETG/8.0 wt.% Si_3N_4, and PETG/10.0 wt.% Si_3N_4 specimens are shown in Figure 10. Information regarding tensile toughness, Charpy impact strength, and M–H is shown in Figure 10a, Figure 10b, and Figure 10c, respectively. In relation to the pure PETG results, the composites with the highest values were PETG/6.0 wt.% Si_3N_4, exhibiting a 15.6% increase for tensile toughness; PETG/8.0 wt.% Si_3N_4, exhibiting an increase of 20.9% with respect to the Charpy impact strength; and the PETG/10.0 wt.% Si_3N_4, exhibiting an increase of 18.8% as to the M-H.
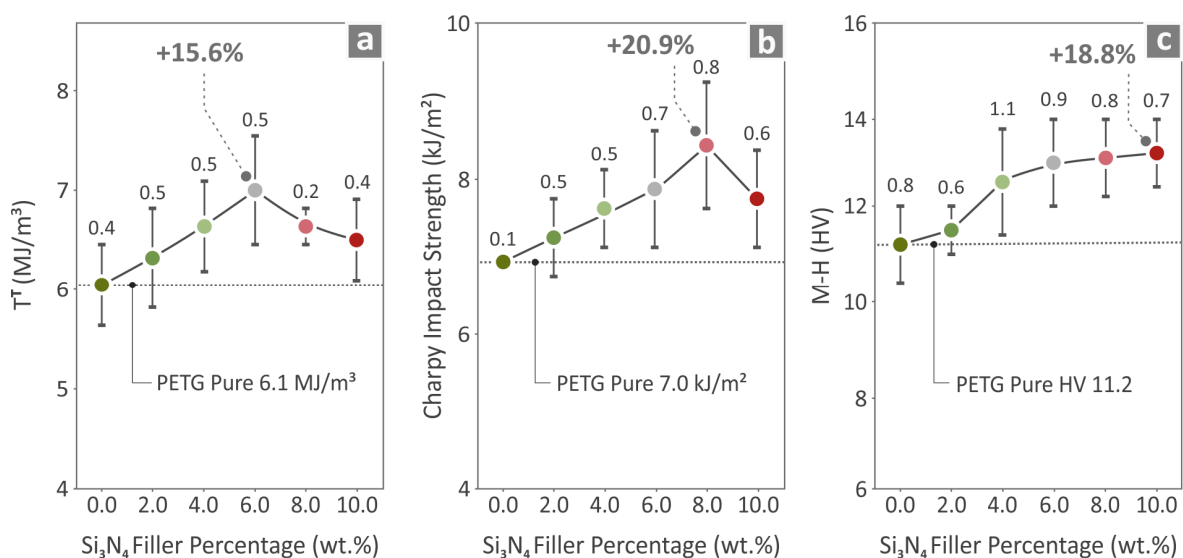

Figure 10. Pure PETG and PETG/x wt.% Si_3N_4 (x = 2.0, 4.0, 6.0, 8.0, and 10.0 wt.%) specimens' values derived from the (**a**) tensile toughness, (**b**) Charpy impact strength, and (**c**) M-H tests.

3.6. Electrical/Dielectric Characterization

The real part of the dielectric permittivity (ε'), the dissipation factor $\tan(\delta)$, and the real part of ac conductivity (σ') as a function of the frequency of the PETG/Si_3N_4 nanocomposites with different filler content (0–10 wt.% Si_3N_4) are shown in Figure 11a–c. The dielectric permittivity of pure PETG showed no considerable frequency dispersion over the measured frequency range; that is, ε' increases gradually from a value of 2.8 at

4 MHz to 3.3 at low frequencies, in accordance with reported values in the literature [77]. The corresponding dissipation factor exhibits values lower than 0.04 over almost the entire measured frequency range. A broad relaxation peak in the tan(δ) spectra was observed at high frequencies, located at approximately 10 kHz. This high-*f* feature remained unaffected by the addition of Si_3N_4 nanoparticles and can be attributed to the relaxation polarization of the polymer matrix [78]. Furthermore, an additional feature developed at low frequencies of approximately 2 Hz, which increased in intensity with an increasing filler content. This low-*f* feature can be attributed to the interfacial polarization caused by the interaction between the polymer matrix and conductive filler particles.
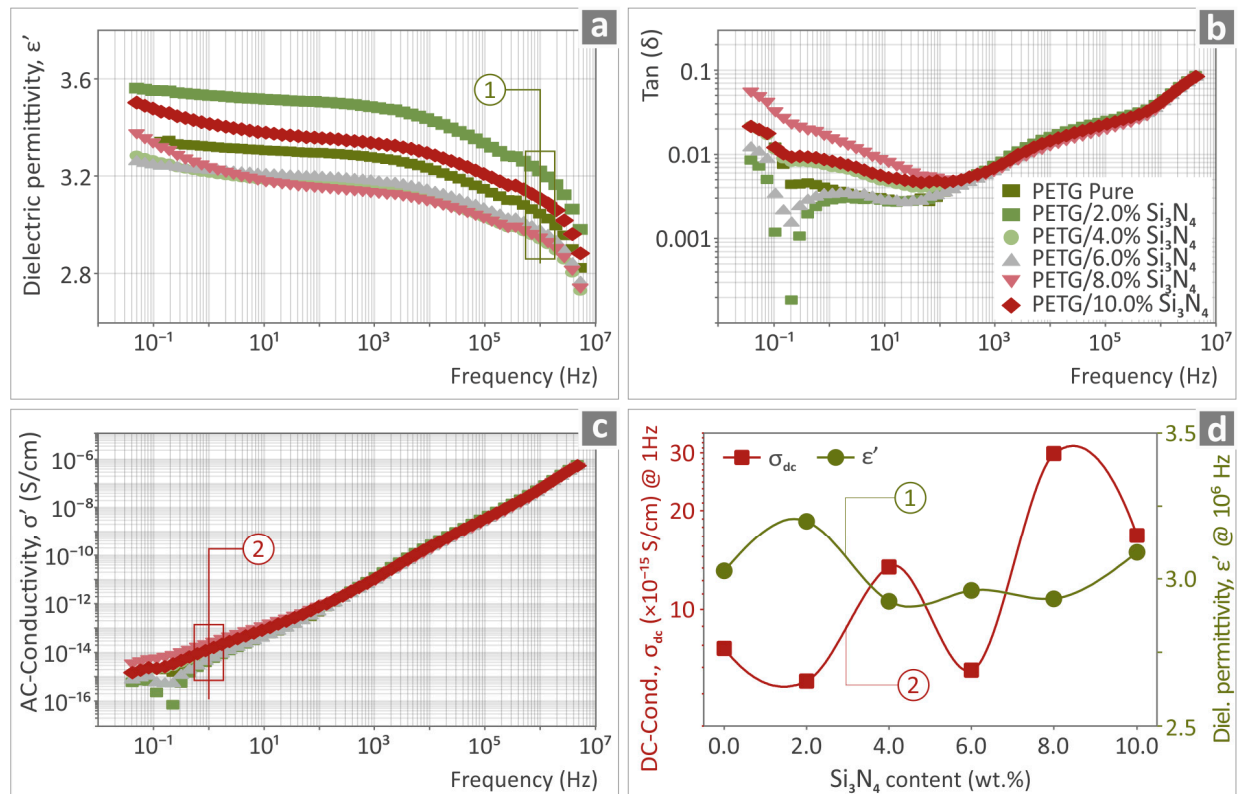

Figure 11. Frequency dependence of (**a**) the real part of dielectric permittivity (ε′), (**b**) the dissipation factor tan(δ), and (**c**) the real part of ac conductivity (σ′) of pure PETG and PETG/x wt.% Si_3N_4 composites at filler proportions ranging from 2 to 10 wt.%. (**d**) DC conductivity (σ_{dc}) measured at 1 Hz and dielectric permittivity, ε_∞ (measured at 1 MHz), as a function of Si_3N_4 content.

When the Si_3N_4 content was increased to 10 wt.%, we did not observe any significant spectral changes in either the dielectric permittivity or the ac-conductivity representation (Figure 11a,c). The permittivity values at high frequencies (ε_∞) exhibited insignificant changes, varying from 2.8. to 3.4, as shown in Figure 11d. The AC conductivity spectra of the pure PETG and PETG/x wt.%Si_3N_4 nanocomposites show the characteristic behavior of insulating materials such as polymers; that is, ac-conductivity scales with ω at high frequencies. In the low-frequency range, a DC plateau began to develop, corresponding to the DC conductivity values of the composites varying from 5×10^{-16} S/cm to 6×10^{-15} S/cm. The variation in conductivity values measured at 1 Hz (dc-conductivity) with an increasing filler content is shown separately in Figure 11d. The above observations suggest that the overall electrical/dielectric behaviors of the PETG/x wt.% Si_3N_4 composites are mainly determined by the properties of the polymer matrix.

3.7. Analysis of Specimens through Micro Computed Tomography (μ-CT) Scanning

In Figure 12a, the dimensional deviation graphs of pure PETG, PETG/2.0 wt.% Si_3N_4, PETG/4.0 wt.% Si_3N_4, PETG/6.0 wt.% Si_3N_4, PETG/8.0 wt.% Si_3N_4, and PETG/10.0 wt.% Si_3N_4 are presented. Figure 12b,c depict color-coded tensile stress test results for PETG/2.0 wt.% Si_3N_4 regarding its dimensional deviation. Figure 12d shows A2N at a 95% dimensional deviation for PETG/2.0 wt.% Si_3N_4, PETG/4.0 wt.% Si_3N_4, PETG/6.0 wt.% Si_3N_4, PETG/8.0 wt.% Si_3N_4, and PETG/10.0 wt.% Si_3N_4 and pure PETG, among which the value of PETG/6.0 wt.% Si_3N_4 was found to be 62.1% below the one corresponding to pure PETG.
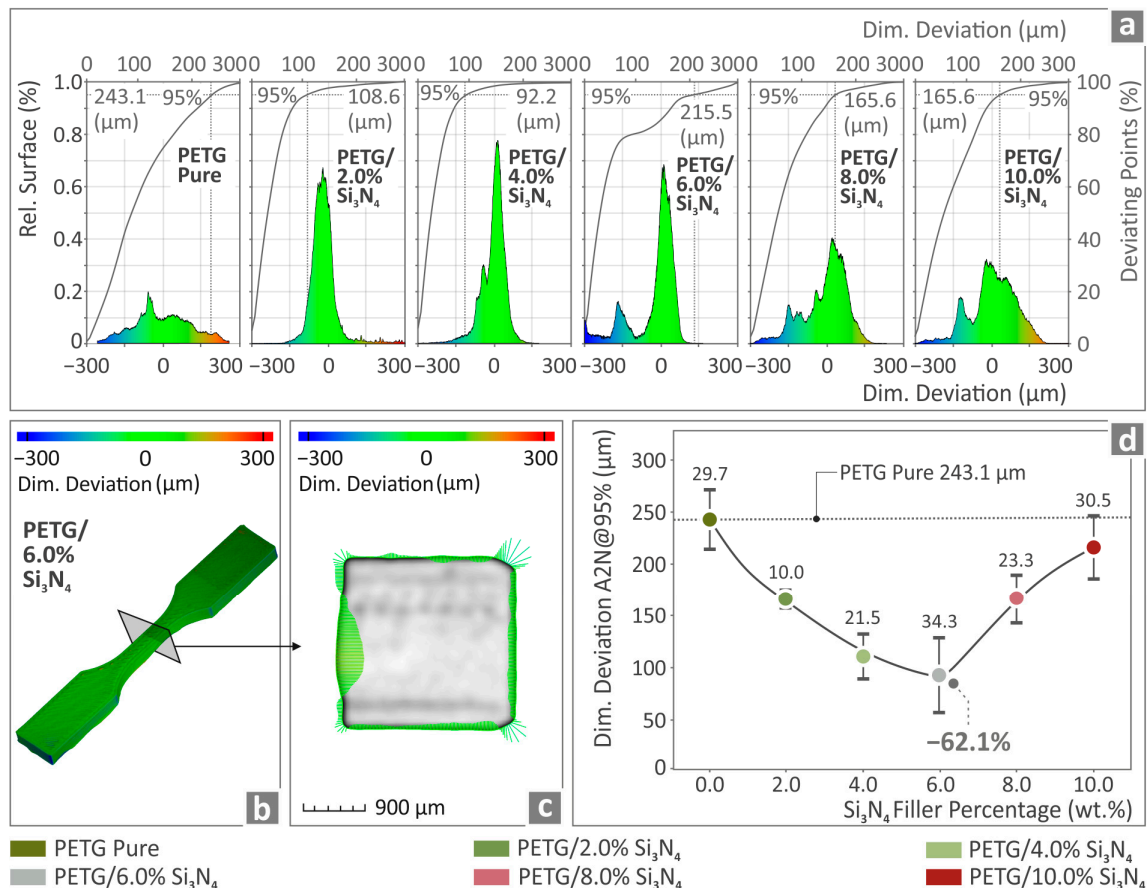

Figure 12. (**a**) Pure PETG and PETG/*x* wt.% Si_3N_4 (*x* = 2.0, 4.0, 6.0, 8.0, and 10.0 wt.%) results as to the curves corresponding to the dimensional deviation of the fabricated specimens. (**b**,**c**) PETG/6.0 wt.% Si_3N_4 tensile stress test results regarding the specimen's structural deviation and (**d**) dimensional deviation A2N at 95% regarding pure PETG and PETG/*x* wt.% Si_3N_4 (*x* = 2.0, 4.0, 6.0, 8.0, and 10.0 wt.%).

Relevant information regarding the void compactness, sphericity, and diameter of such characteristics for the various specimens is shown in Figure 13a for the pure PETG and all PETG/*x* wt.% Si_3N_4 composites. The results for the PETG/6.0 wt.% Si_3N_4 composite are illustrated in Figures 13b and 13c, respectively, in which they are color-coded regarding voids, while the porosity percentages of pure PETG and the PETG/*x* wt.% Si_3N_4 with *x* = 2.0, 4.0, 6.0, 8.0, and 10.0 wt.% composites are presented in Figure 13d. It can be observed that the *x* = 4.0 wt.% Si_3N_4 composite presented the most promising results, being 48.5% lower than the value corresponding to pure PETG.
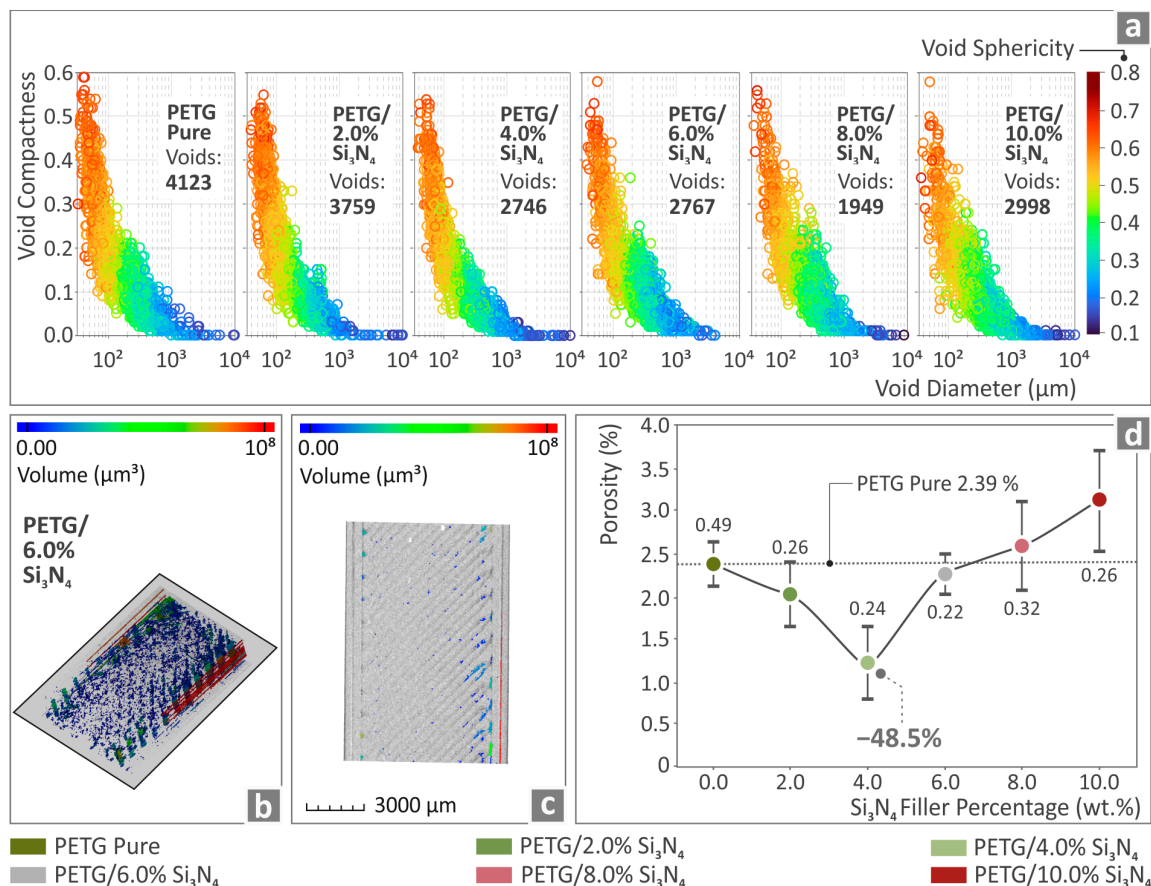
Figure 13. (**a**) Pure PETG and PETG/*x* wt.% Si_3N_4 (*x* = 2.0, 4.0, 6.0, 8.0, and 10.0 wt.%) results regarding void compactness sphericity and diameter of the fabricated specimens. (**b**,**c**) PETG/6.0 wt.% Si_3N_4 sample porosity in color-coding mapping and (**d**) porosity percentage regarding pure PETG and PETG/*x* wt.% Si_3N_4 (*x* = 2.0, 4.0, 6.0, 8.0, and 10.0 wt.%).

3.8. Analysis of Specimens through Scanning Electron Microscopy

The mechanically tested specimens were subjected to SEM analysis, and relevant images of their sides and fracture surfaces are shown in Figure 14. Figure 14a,d,g depict the side surfaces of the pure PETG, PETG/4.0 wt.% Si_3N_4, and PETG/8.0 wt.% Si_3N_4, respectively, magnified 150×, indicating good layering of the material without defects. Figure 14b,e,h show the fracture surfaces of the pure PETG, PETG/4.0 wt.% Si_3N_4, and PETG/8.0 wt.% Si_3N_4 specimens, respectively, magnified 30×, presenting a solid layering with some voids. The same samples are presented in Figure 14c,f,i, where the fractured surfaces are magnified 1000×, and their high quality can be observed and confirmed, as no defects appear to be present.

Side surface images of a PETG/10.0 wt.% Si_3N_4 specimen can be observed in Figure 15a,b, magnified at 30× and at 150× respectively, indicating great layer fusion. Figure 15c shows an EDS mapping image, while Figure 15d–f present the fracture surface images of PETG/10.0 wt.% Si_3N_4 at 30×, 1000×, and 30,000× magnifications, respectively. The revealed structure was determined to be of high quality because the defects and voids were minimal, except in the case of Figure 15f, where some areas showed uneven pieces of material.
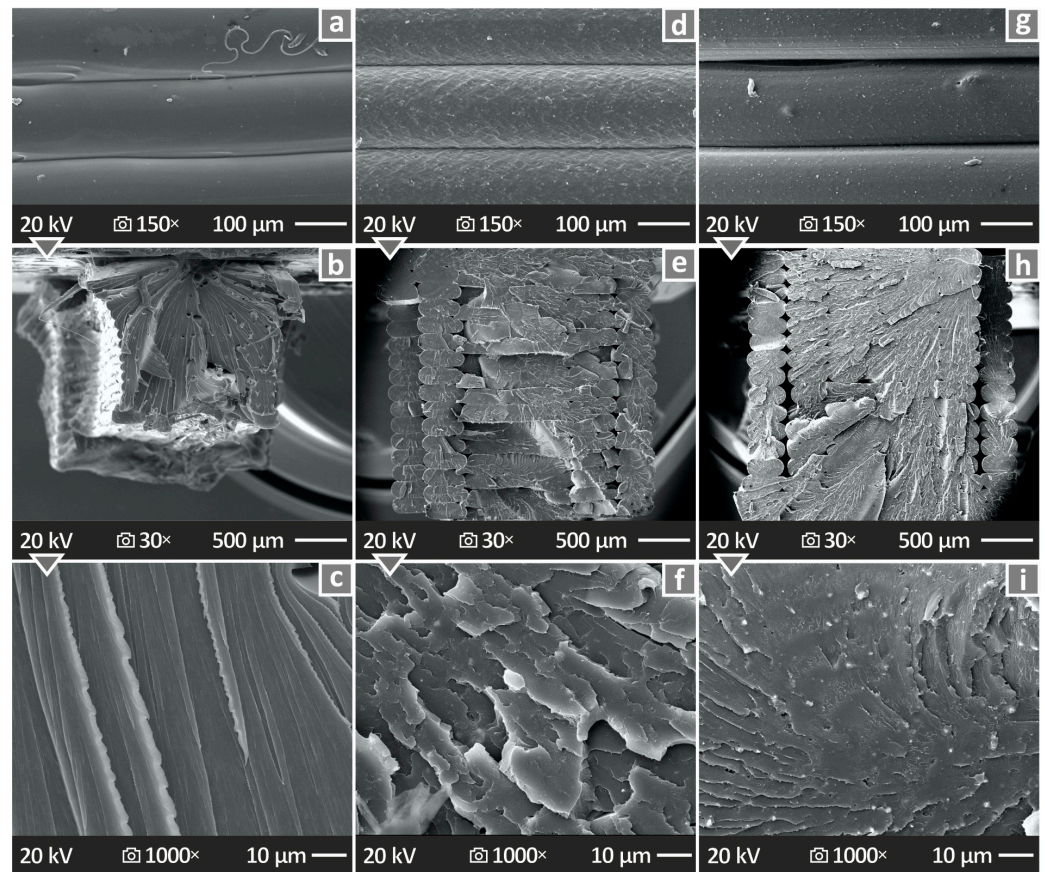
Figure 14. Depiction of the surfaces of the pure PETG, PETG/4.0 wt.% Si_3N_4, and PETG/8.0 wt.% Si_3N_4 samples through SEM, namely, (**a**,**d**,**g**) their side surfaces magnified 150×, (**b**,**e**,**h**) their fracture surfaces at 30× magnification, and (**c**,**f**,**i**) their fracture surfaces at 1000× magnification.
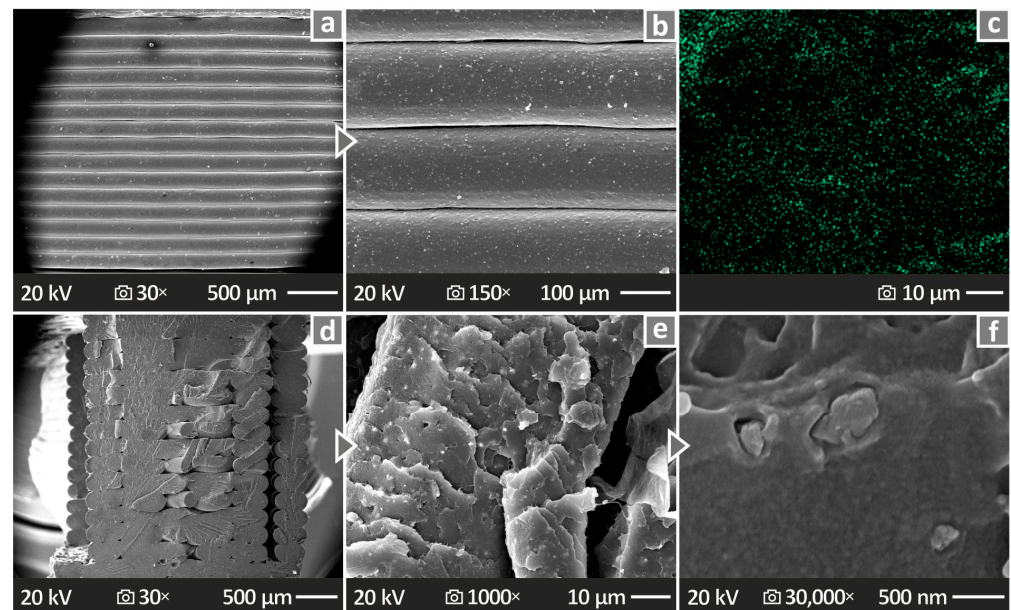

Figure 15. (**a**,**b**) Depiction of the PETG/10.0 wt.% Si_3N_4 sample's side surface via SEM, magnified at 30× and 150×, respectively; (**c**) EDS mapping picture of a chosen sample; (**d**–**f**) depiction of the PETG/10.0 wt.% Si_3N_4 sample's fracture surface via SEM, magnified at 30×, 1000×, and 30,000×, respectively.

4. Discussion

The authors used a typical thermomechanical process for filament preparation, constituting the standard in the industry for both pure polymeric materials and composites. They chose to use this approach as it can easily be scaled up and industrialized. The drying process was used to remove any remaining moisture from the atmosphere first from the raw materials and the filament afterward. This is also a typical method and entails removing moisture from the atmosphere. The production of the filament did not include any solutions or other liquids that would need to be removed using filtration processes afterward. Additionally, a thorough process was followed to ensure the quality of the produced filament, as presented in this manuscript. This included inspection of random parts of the filament under a microscope to locate possible defects and qualitatively evaluate its surface roughness, measuring its diameter, and finally conducting tensile tests to assess its strength. In the mechanical tests, no high deviations were found between the samples, indicating a similar composition and structure between the filament samples. The tensile test results are comparable to those of the respective 3D printed samples, although such a comparison cannot be considered reliable. The filaments were not tested according to a standard, as the authors are not aware of such a standard for filament tensile testing.

The findings on the mechanical properties revealed reinforcement in relation to the behavior of pure PETG, especially for a 6.0 wt.% Si_3N_4 filler percentage, which presented the most enhanced properties among all the various composites synthesized. The dielectric properties were examined, and the results suggested that the polymer matrix mainly affected overall electrical behavior. The structures of the specimens were observed using an electron microscope (SEM) at various magnifications. These SEM images show the very good layering and inner structures of the various specimens, which were not negatively affected by the addition of different filler percentages of Si_3N_4. The dimensional deviation results were significant in the case of the 6.0 wt.% Si_3N_4 composite, while in the case of 4.0 wt.% Si_3N_4, the porosity percentage was the lowest among all the different composites synthesized. The EDS analysis showed a relatively good dispersion of the additive, which verified the excellent results for sample structure derived from the rest of the tests. On the left side of Figure 16, the spider graph shows all the mechanical properties of the PETG/x wt.% Si_3N_4 and pure PETG samples, whereas on the right side of Figure 16, the mechanical properties are matched with the composites in which their greatest values were detected. This enhancement in the mechanical properties can be attributed to the interactions between the nanoparticles and the matrix as well as the restriction of polymer chain mobility resulting from the nanoparticles occupying the spaces between them [79–81].

Regarding the physical properties, rheology was affected, as discussed. This has an effect on the 3D-printed structure, which provides information for the optimization of the 3D-printing settings for each composite to maximize mechanical performance. For comparison purposes, this optimization was not performed in this study. Regarding the brittleness of the samples, no large differences were found between the unfilled PETG and the nanocomposites. The inspection of the fracture surfaces showed minimum deformation in both the pure PETG and the nanocomposites. At the same time, the 3D-printed samples failed at similar strain values for tensile strength. Only the higher-loaded samples failed at lower strain values, revealing inferior mechanical strength. This can be attributed to the saturation of the filler in the matrix, which negatively affects mechanical performance [79,82].

It is important to highlight that the scanning electron microscopy (SEM) images displayed finely crafted surfaces and a uniformly distributed layering of the materials, even after the addition of fillers. A few voids were detected, and any defects observed were minimal in size. The incorporation of Si_3N_4 nanoparticles influenced the rheological behavior of the PETG polymer, resulting in an overall increase in viscosity. The MFR increased to 4 wt.% Si_3N_4 content in the composites and drastically reduced at higher loadings. Despite these changes, there were no significant disparities in the quality of the 3D-printed parts. The fusion of layers, as evidenced by the images of the lateral

surfaces, appeared to remain intact, even for the higher-loaded nanocomposites, indicating a consistent layer thickness.
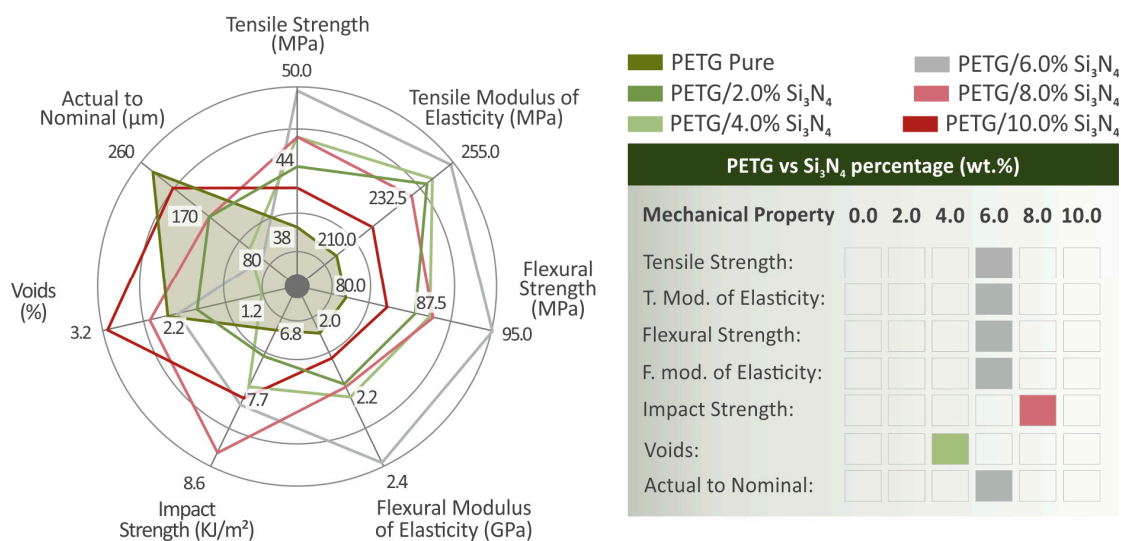

Figure 16. (**On the left side of the figure**) The examined mechanical properties' values are summarized in a spider graph regarding pure PETG and PETG/*x* wt.% Si$_3$N$_4$ (*x* = 2.0, 4.0, 6.0, 8.0, and 10.0 wt.%). (**On the right side of the figure**) Data board highlighting the composites wherein each mechanical property presented the greatest result.

Inspection of the internal structure via micro-computed tomography (μ-CT) corroborated these findings. The addition of Si$_3$N$_4$ enhanced dimensional accuracy and reduced the number of voids in the internal structure. Notably, nanocomposites with superior mechanical performance exhibited fewer voids and better dimensional accuracy, implying a correlation between printing quality and mechanical strength. This is in agreement with the literature, which indicates that increased porosity negatively affects the mechanical performance of 3D-printed parts [83,84]. In contrast, the addition of 4 wt.% composite showed the minimum porosity among the samples tested, showing that other factors affected the mechanical strength of the samples besides porosity. The 6 wt.% composite showed the best dimensional accuracy among the samples assessed, which is an indication of good 3D-printing quality as well, showing that good 3D-printing quality positively affects the mechanical performance of the 3D-printed parts.

The thermal property analysis indicated that there was a negligible impact of Si$_3$N$_4$ addition on the PETG response to high temperatures, confirming the safety of the temperature levels used and the absence of thermal degradation. Tg increased only slightly in the composites with higher filler loadings. SEM and energy-dispersive X-ray spectroscopy (EDS) did not reveal major particle clustering in the fracture surfaces, even in the higher-loaded composites. No agglomerations were located in the nanocomposites with lower Si$_3$N$_4$ content. Moreover, the mechanical tests revealed that the deviation in results remained within acceptable limits, which suggests that the composition of the nanocompounds was consistent across all the examined samples. Therefore, it is safe to assume that a good dispersion of Si$_3$N$_4$ nanoparticles in the PETG matrix was achieved using the process followed for the preparation of the nanocomposites. The raw material mixing process and the filament extruder used, the latter of which is specially optimized for material mixing, contributed to this result. Even the highest-loaded samples exhibited slightly superior mechanical performance compared to pure PETG. A decreasing trend was found, indicating possible saturation of the filler, although the saturation threshold of the Si$_3$N$_4$ filler in the matrix was not precisely determined, as such information fell outside the scope of this study.

After reviewing the related literature, similar investigations were performed to examine Si_3N_4 as a filler and its reinforcing properties in nanocomposites. In ref. [85], Si_3N_4 was employed as an additive in the matrix material of polypropylene (PP) to investigate its effect on the mechanical and electrical properties of PP, as also observed in this study, in which PETG was used as the matrix material. The results indicate an increase in impact strength and a decrease in tensile strength, which is in disagreement with the tensile strength results of the study. This behavior may be attributed to the different matrix materials used in each study.

In another study [60], Si_3N_4 was added to two polymer matrix materials: high-density polyethylene (HDPE) and polypropylene. The 3D-printed parts of the polymer–ceramic material presented smooth surfaces without ledges or discontinuous areas, a result that was also observed in the samples in this study. Moreover, the filler content of 10 wt.% did not cause any remarkable reinforcement of the elastic modulus, and the critical strain decreased. In ref. [42], biomedical-grade PLA with various filler loadings was employed as a matrix material for Si_3N_4. A series of tests were conducted on the composites, indicating an increase in flexural and tensile strength, as also observed in the present work. In Table 3 below, a comparison of the effects of Si_3N_4 as a reinforcement agent on different polymeric matrices is presented. As shown, there are differences in the performance of Si_3N_4 as a reinforcement agent between the polymeric matrices, but overall, the results can be considered comparable. Any differences can be attributed to the different polymeric matrices used and the differences in the preparation process of the composites.

Table 3. Comparison with the literature regarding the findings on the effect of using Si_3N_4 as an additive in polymeric matrices on mechanical properties.

	Current Study	**[42] (PLA Matrix)**	**[55] (ABS Matrix)**	**[59] (PP Matrix)**	**[85] (PP Matrix)**
Impact strength increase	20.9%	30.2%	Decrease	11.1%	25%
Tensile strength increase	24.5%	40.4%	25.6%	16%	Decrease
Flexural strength increase	16.6%	33.2%	30.3%	15.7%	-
microhardness	18.8%	20.9%	34.9%	33.6%	-

5. Conclusions

Composites consisting of PETG and Si_3N_4 were synthesized in appropriate mixtures and used to produce filaments suitable for the fabrication of various specimens using MEX 3D-P. Specifically, composites with 2.0, 4.0, 6.0, 8.0, and 10.0 wt.% Si_3N_4 filler quantities were shaped into mixtures, filaments, and finally specimens. Samples originating from the raw materials, the filaments, and the final 3D-P specimens underwent specific tests, with the aim of investigating their properties and performance under specific conditions. SEM was used to investigate the structures of all the specimens. An EDS analysis was conducted to examine the chemical compositions of the composites and raw Si_3N_4 to reveal the expected chemical elements, thus confirming the quality and homogeneity of the prepared materials. The electrical and dielectric properties pertaining to BDS were investigated. Raman spectroscopy, TGA, and differential scanning calorimetry (DSC) were performed. The viscosities and MFR were also investigated. The tensile performance of the filaments was tested. A similar experiment was performed on the specimens to determine their flexural properties, Charpy impact strength, and microhardness. The dimensional deviation and void percentages of the various samples were also examined.

The derived results revealed a remarkable enhancement in PETG/6.0 wt.% Si_3N_4 performance for the majority of the properties. Additional work could include observing the influence of different 3D-P settings on the performance of the samples. Thus, elucidating the influence of 3D-P settings on the overall performance of the final products can have a tremendous impact on the creation of various parts used in anti-ballistic protection [86], including various armor parts used in personal protective gear, such as helmets, breastplates, or joint protective gear for kneepads and elbows. All of the above can have a significant

positive impact on the defense and security industry, revolutionizing applications and reducing manufacturing costs significantly.

Author Contributions: N.M. (Nikolaos Michailidis): validation, visualization, and formal analysis; M.P.: writing—review and editing; V.S.: formal analysis, data curation; V.P.: visualization and validation; M.S.: writing—original draft preparation; N.M. (Nikolaos Mountakis): data curation and visualization; A.A.: formal analysis and data curation; J.V.: formal analysis and data curation; N.K.N.: investigation and writing—original draft preparation; N.V.: conceptualization, methodology, resources, supervision, and project administration. The manuscript was written with contributions from all the authors. All authors have read and agreed to the published version of the manuscript.

References

1. Jacobs, P.F. *Rapid Prototyping & Manufacturing: Fundamentals of Stereolithography*; Society of Manufacturing Engineers: Dearborn, MI, USA, 1992.
2. Comb, J.W.; Priedeman, W.R.; Turley, P.W. FDM® Technology Process Improvements. In Proceedings of the 1994 International Solid Freeform Fabrication Symposium, Austin, TX, USA. Available online: http://hdl.handle.net/2152/68588 (accessed on 20 December 2023).
3. Sachs, E.M.; Haggerty, J.S.; Cima, M.J.; Williams, P.A. Three-Dimensional Printing Techniques. U.S. Patent 5,204,055, 20 April 1993.
4. Beaman, J.J.; Barlow, J.W.; Bourell, D.L.; Crawford, R.H.; Marcus, H.L.; McAlea, K.P. *Solid Freeform Fabrication: A New Direction in Manufacturing*; Springer: Boston, MA, USA, 1997; ISBN 978-0-7923-9834-9.
5. Feygin, M.; Hsieh, B. Laminaled Objecf Manufacturing (Lom): A Simpler Process. In Proceedings of the 1991 International Solid Freeform Fabrication Symposium, Austin, TX, USA. Available online: http://hdl.handle.net/2152/64325 (accessed on 20 December 2023).
6. Mazumder, J.; Schifferer, A.; Choi, J. Direct Materials Deposition: Designed Macro and Microstructure. *Mater. Res. Innov.* **1999**, *3*, 118–131. [CrossRef]
7. Guo, N.; Leu, M.C. Additive Manufacturing: Technology, Applications and Research Needs. *Front. Mech. Eng.* **2013**, *8*, 215–243. [CrossRef]
8. Attaran, M. The Rise of 3-D Printing: The Advantages of Additive Manufacturing over Traditional Manufacturing. *Bus. Horiz.* **2017**, *60*, 677–688. [CrossRef]
9. Sepasgozar, S.M.E.; Shi, A.; Yang, L.; Shirowzhan, S.; Edwards, D.J. Additive Manufacturing Applications for Industry 4.0: A Systematic Critical Review. *Buildings* **2020**, *10*, 231. [CrossRef]
10. Thomas, C.L.; Gaffney, T.M.; Kaza, S.; Lee, C.H. Rapid Prototyping of Large Scale Aerospace Structures. In Proceedings of the 1996 IEEE Aerospace Applications Conference, Aspen, CO, USA, 10 February 1996; pp. 219–230.
11. Bacciaglia, A.; Ceruti, A.; Liverani, A. Towards Large Parts Manufacturing in Additive Technologies for Aerospace and Automotive Applications. *Procedia Comput. Sci.* **2022**, *200*, 1113–1124. [CrossRef]
12. Mohanavel, V.; Ashraff Ali, K.S.; Ranganathan, K.; Allen Jeffrey, J.; Ravikumar, M.M.; Rajkumar, S. The Roles and Applications of Additive Manufacturing in the Aerospace and Automobile Sector. *Mater. Today Proc.* **2021**, *47*, 405–409. [CrossRef]
13. Najmon, J.C.; Raeisi, S.; Tovar, A. Review of Additive Manufacturing Technologies and Applications in the Aerospace Industry. In *Additive Manufacturing for the Aerospace Industry*; Elsevier: Amsterdam, The Netherlands, 2019; pp. 7–31.
14. Tepylo, N.; Huang, X.; Patnaik, P.C. Laser-Based Additive Manufacturing Technologies for Aerospace Applications. *Adv. Eng. Mater.* **2019**, *21*, 1900617. [CrossRef]
15. de Leon, A.C.; Chen, Q.; Palaganas, N.B.; Palaganas, J.O.; Manapat, J.; Advincula, R.C. High Performance Polymer Nanocomposites for Additive Manufacturing Applications. *React. Funct. Polym.* **2016**, *103*, 141–155. [CrossRef]
16. Song, Y.; Yan, Y.; Zhang, R.; Xu, D.; Wang, F. Manufacture of the Die of an Automobile Deck Part Based on Rapid Prototyping and Rapid Tooling Technology. *J. Mater. Process Technol.* **2002**, *120*, 237–242. [CrossRef]

17. Vasco, J.C. Additive Manufacturing for the Automotive Industry. In *Additive Manufacturing*; Elsevier: Amsterdam, The Netherlands, 2021; pp. 505–530.

18. Sun, C.; Wang, Y.; McMurtrey, M.D.; Jerred, N.D.; Liou, F.; Li, J. Additive Manufacturing for Energy: A Review. *Appl. Energy* **2021**, *282*, 116041. [CrossRef]

19. Cramer, C.L.; Ionescu, E.; Graczyk-Zajac, M.; Nelson, A.T.; Katoh, Y.; Haslam, J.J.; Wondraczek, L.; Aguirre, T.G.; LeBlanc, S.; Wang, H.; et al. Additive Manufacturing of Ceramic Materials for Energy Applications: Road Map and Opportunities. *J. Eur. Ceram. Soc.* **2022**, *42*, 3049–3088. [CrossRef]

20. Goh, G.L.; Zhang, H.; Chong, T.H.; Yeong, W.Y. 3D Printing of Multilayered and Multimaterial Electronics: A Review. *Adv. Electron. Mater.* **2021**, *7*, 141–155. [CrossRef]

21. Zhang, Z.; Yuan, X. Applications and Future of Automated and Additive Manufacturing for Power Electronics Components and Converters. *IEEE J. Emerg. Sel. Top. Power Electron.* **2022**, *10*, 4509–4525. [CrossRef]

22. Colorado, H.A.; Cardenas, C.A.; Gutierrez-Velazquez, E.I.; Escobedo, J.P.; Monteiro, S.N. Additive Manufacturing in Armor and Military Applications: Research, Materials, Processing Technologies, Perspectives, and Challenges. *J. Mater. Res. Technol.* **2023**, *27*, 3900–3913. [CrossRef]

23. Busachi, A.; Erkoyuncu, J.; Colegrove, P.; Martina, F.; Watts, C.; Drake, R. A Review of Additive Manufacturing Technology and Cost Estimation Techniques for the Defence Sector. *CIRP J. Manuf. Sci. Technol.* **2017**, *19*, 117–128. [CrossRef]

24. Giannatsis, J.; Dedoussis, V. Additive Fabrication Technologies Applied to Medicine and Health Care: A Review. *Int. J. Adv. Manuf. Technol.* **2009**, *40*, 116–127. [CrossRef]

25. Ovsianikov, A. Additive Manufacturing Technologies for Biomedical Applications. Professorial Dissertation, Technische Universität Wien, Vienna, Austria, 2017. Available online: http://hdl.handle.net/20.500.12708/159459 (accessed on 20 December 2023).

26. Chauhan, I.; Chattopadhyay, S.; Mohanty, P. Fabrication of Titania Nanowires Incorporated Paper Sheets and Study of Their Optical Properties. *Mater. Express* **2013**, *3*, 343–349. [CrossRef]

27. Hwa, L.C.; Uday, M.B.; Ahmad, N.; Noor, A.M.; Rajoo, S.; Zakaria, K. Bin Integration and Fabrication of the Cheap Ceramic Membrane through 3D Printing Technology. *Mater. Today Commun.* **2018**, *15*, 134–142. [CrossRef]

28. Fichou, D.; Morlock, G.E. Open-Source-Based 3D Printing of Thin Silica Gel Layers in Planar Chromatography. *Anal. Chem.* **2017**, *89*, 2116–2122. [CrossRef] [PubMed]

29. Ahmed, W.; Siraj, S.; Al-Marzouqi, A.H. Embracing Additive Manufacturing Technology through Fused Filament Fabrication for Antimicrobial with Enhanced Formulated Materials. *Polymers* **2021**, *13*, 1523. [CrossRef] [PubMed]

30. Velu, R.; Jayashankar, D.K.; Subburaj, K. Additive Processing of Biopolymers for Medical Applications. In *Additive Manufacturing*; Elsevier: Amsterdam, The Netherlands, 2021; pp. 635–659.

31. Yasa, E.; Ersoy, K. Dimensional Accuracy and Mechanical Properties of Chopped Carbon Reinforced Polymers Produced by Material Extrusion Additive Manufacturing. *Materials* **2019**, *12*, 3885. [CrossRef] [PubMed]

32. Vidakis, N.; Mangelis, P.; Petousis, M.; Mountakis, N.; Papadakis, V.; Moutsopoulou, A.; Tsikritzis, D. Mechanical Reinforcement of ABS with Optimized Nano Titanium Nitride Content for Material Extrusion 3D Printing. *Nanomaterials* **2023**, *13*, 669. [CrossRef] [PubMed]

33. Vidakis, N.; Petousis, M.; Tzounis, L.; Velidakis, E.; Mountakis, N.; Grammatikos, S.A. Polyamide 12/Multiwalled Carbon Nanotube and Carbon Black Nanocomposites Manufactured by 3D Printing Fused Filament Fabrication: A Comparison of the Electrical, Thermoelectric, and Mechanical Properties. *C* **2021**, *7*, 38. [CrossRef]

34. García Plaza, E.; Núñez López, P.; Caminero Torija, M.; Chacón Muñoz, J. Analysis of PLA Geometric Properties Processed by FFF Additive Manufacturing: Effects of Process Parameters and Plate-Extruder Precision Motion. *Polymers* **2019**, *11*, 1581. [CrossRef] [PubMed]

35. Bouzaglou, O.; Golan, O.; Lachman, N. Process Design and Parameters Interaction in Material Extrusion 3D Printing: A Review. *Polymers* **2023**, *15*, 2280. [CrossRef] [PubMed]

36. Devsingh, D.; Dev, A.D.; Avala, B.; Reddy, R.; Arjula, S. Characterization of Additive Manufactured PETG and Carbon Fiber-PETG. *Int. J. Res. Eng. Appl. Manag. (IJREAM)* **2018**, *4*, 2. [CrossRef]

37. Valvez, S.; Silva, A.P.; Reis, P.N.B. Optimization of Printing Parameters to Maximize the Mechanical Properties of 3D-Printed PETG-Based Parts. *Polymers* **2022**, *14*, 2564. [CrossRef] [PubMed]

38. Vidakis, N.; Petousis, M.; Tzounis, L.; Grammatikos, S.A.; Porfyrakis, E.; Maniadi, A.; Mountakis, N. Sustainable Additive Manufacturing: Mechanical Response of Polyethylene Terephthalate Glycol over Multiple Recycling Processes. *Materials* **2021**, *14*, 1162. [CrossRef]

39. Latko-Durałek, P.; Dydek, K.; Boczkowska, A. Thermal, Rheological and Mechanical Properties of PETG/RPETG Blends. *J. Polym. Env.* **2019**, *27*, 2600–2606. [CrossRef]

40. Szykiedans, K.; Credo, W.; Osiński, D. Selected Mechanical Properties of PETG 3-D Prints. *Procedia Eng.* **2017**, *177*, 455–461. [CrossRef]

41. Yan, C.; Kleiner, C.; Tabigue, A.; Shah, V.; Sacks, G.; Shah, D.; DeStefano, V. PETG: Applications in Modern Medicine. *Eng. Regen.* **2024**, *5*, 45–55. [CrossRef]

42. Vidakis, N.; Petousis, M.; Michailidis, N.; Papadakis, V.; Mountakis, N.; Argyros, A.; Dimitriou, E.; Charou, C.; Moutsopoulou, A. Polylactic Acid/Silicon Nitride Biodegradable and Biomedical Nanocomposites with Optimized Rheological and Thermomechanical Response for Material Extrusion Additive Manufacturing. *Biomed. Eng. Adv.* **2023**, *6*, 100103. [CrossRef]

43. Antoniadis, A.; Vidakis, N.; Bilalis, N. Fatigue Fracture Investigation of Cemented Carbide Tools in Gear Hobbing, Part 2: The Effect of Cutting Parameters on the Level of Tool Stresses—A Quantitative Parametric Analysis. *J. Manuf. Sci. Eng.* **2002**, *124*, 792–798. [CrossRef]

44. Bouzakis, K.-D.; Vidakis, N.; Kallinikidis, D.; Leyendecker, T.; Erkens, G.; Wenke, R.; Fuss, H.-G. Fatigue Failure Mechanisms of Multi- and Monolayer Physically Vapour-Deposited Coatings in Interrupted Cutting Processes. *Surf. Coat. Technol.* **1998**, *108–109*, 526–534. [CrossRef]

45. Wang, F.; Guo, J.; Li, K.; Sun, J.; Zeng, Y.; Ning, C. High Strength Polymer/Silicon Nitride Composites for Dental Restorations. *Dent. Mater.* **2019**, *35*, 1254–1263. [CrossRef] [PubMed]

46. Correa Filho, L.; Fu, L.; Engqvist, H.; Xia, W.; Persson, C. Wear Performance of a Novel Silicon Nitride Ceramic for Biomedical Applications. *Biomed. Mater. Devices* **2023**, *1*, 990–999. [CrossRef]

47. Khan, A.; Puttegowda, M.; Jagadeesh, P.; Marwani, H.M.; Asiri, A.M.; Manikandan, A.; Parwaz Khan, A.A.; Ashraf, G.M.; Rangappa, S.M.; Siengchin, S. Review on Nitride Compounds and Its Polymer Composites: A Multifunctional Material. *J. Mater. Res. Technol.* **2022**, *18*, 2175–2193. [CrossRef]

48. Bouzakis, K.-D.; Vidakis, N.; Lontos, A.; Mitsi, S.; David, K. Implementation of Low Temperature-Deposited Coating Fatigue Parameters in Commercial Roller Bearings Catalogues. *Surf. Coat. Technol.* **2000**, *133–134*, 489–496. [CrossRef]

49. Bouzakis, K.-D.; Vidakis, N.; Mitsi, S. Fatigue Prediction of Thin Hard Coatings on the Steel Races of Hybrid Bearings Used in High Speed Machine Tool Spindles. *J. Tribol.* **1998**, *120*, 835–842. [CrossRef]

50. Krstic, Z.; Krstic, V.D. Silicon Nitride: The Engineering Material of the Future. *J. Mater. Sci.* **2012**, *47*, 535–552. [CrossRef]

51. Riley, F.L. Silicon Nitride and Related Materials. *J. Am. Ceram. Soc.* **2000**, *83*, 245–265. [CrossRef]

52. Bodišová, K.; Kašiarová, M.; Domanická, M.; Hnatko, M.; Lenčéš, Z.; Nováková, Z.V.; Vojtaššák, J.; Gromošová, S.; Šajgalík, P. Porous Silicon Nitride Ceramics Designed for Bone Substitute Applications. *Ceram. Int.* **2013**, *39*, 8355–8362. [CrossRef]

53. Yan, H.; Tang, Y.; Su, J.; Yang, X. Enhanced Thermal–Mechanical Properties of Polymer Composites with Hybrid Boron Nitride Nanofillers. *Appl. Phys. A* **2014**, *114*, 331–337. [CrossRef]

54. Li, M.; Wang, M.; Hou, X.; Zhan, Z.; Wang, H.; Fu, H.; Lin, C.-T.; Fu, L.; Jiang, N.; Yu, J. Highly Thermal Conductive and Electrical Insulating Polymer Composites with Boron Nitride. *Compos. B Eng.* **2020**, *184*, 107746. [CrossRef]

55. Petousis, M.; Michailidis, N.; Papadakis, V.M.; Korlos, A.; Mountakis, N.; Argyros, A.; Dimitriou, E.; Charou, C.; Moutsopoulou, A.; Vidakis, N. Optimizing the Rheological and Thermomechanical Response of Acrylonitrile Butadiene Styrene/Silicon Nitride Nanocomposites in Material Extrusion Additive Manufacturing. *Nanomaterials* **2023**, *13*, 1588. [CrossRef] [PubMed]

56. Badran, Z.; Struillou, X.; Hughes, F.J.; Soueidan, A.; Hoornaert, A.; Ide, M. Silicon Nitride (Si3N4) Implants: The Future of Dental Implantology? *J. Oral. Implantol.* **2017**, *43*, 240–244. [CrossRef] [PubMed]

57. Du, X.; Ronayne, S.; Lee, S.S.; Hendry, J.; Hoxworth, D.; Bock, R.; Ferguson, S.J. 3D-Printed PEEK/Silicon Nitride Scaffolds with a Triply Periodic Minimal Surface Structure for Spinal Fusion Implants. *ACS Appl. Bio Mater.* **2023**, *6*, 3319–3329. [CrossRef] [PubMed]

58. Yunsheng, D.; Hui, X.; Jie, W.; Tingting, Y.; Naiqi, K.; Jiaxing, H.; Wei, C.; Yufei, L.; Qiang, Y.; Shufang, W. Sustained Release Silicon from 3D Bioprinting Scaffold Using Silk/Gelatin Inks to Promote Osteogenesis. *Int. J. Biol. Macromol.* **2023**, *234*, 123659. [CrossRef] [PubMed]

59. Vidakis, N.; Michailidis, N.; Argyros, A.; Mountakis, N.; Papadakis, V.; Spiridaki, M.; Moutsopoulou, A.; Sfakiotakis, E.; Petousis, M. A Coherent Optimization Course of the Silicon Nitride Nanofiller Load in Medical Grade Isotactic Polypropylene for Material Extrusion Additive Manufacturing: Rheology, Engineering Response, and Cost-Effectiveness. *Colloid. Polym. Sci.* **2024**. [CrossRef]

60. Zgalat-Lozynskyy, O.B.; Matviichuk, O.O.; Tolochyn, O.I.; Ievdokymova, O.V.; Zgalat-Lozynska, N.O.; Zakiev, V.I. Polymer Materials Reinforced with Silicon Nitride Particles for 3D Printing. *Powder Metall. Met. Ceram.* **2021**, *59*, 515–527. [CrossRef]

61. Vidakis, N.; Petousis, M.; Michailidis, N.; David, C.; Saltas, V.; Sagris, D.; Spiridaki, M.; Argyros, A.; Mountakis, N.; Papadakis, V. Interpretation of the Optimization Course of Silicon Nitride Nano-Powder Content in Biomedical Resins for Vat Photopolymerization Additive Manufacturing. *Ceram. Int.* **2024**, *50*, 14919–14935. [CrossRef]

62. Wang, M.; Xie, C.; He, R.; Ding, G.; Zhang, K.; Wang, G.; Fang, D. Polymer-Derived Silicon Nitride Ceramics by Digital Light Processing Based Additive Manufacturing. *J. Am. Ceram. Soc.* **2019**, *102*, 5117–5126. [CrossRef]

63. *ASTM D638-02a*; Standard Test Method for Tensile Properties Of Plastics. American Society for Testing and Materials (ASTM International): West Conshohocken, PA, USA, 2003.

64. *ASTM D790-10*; Standard Test Methods for Flexural Properties of Unreinforced and Reinforced Plastics and Electrical Insulating Materials. American Society for Testing and Materials (ASTM International): West Conshohocken, PA, USA, 2016.

65. *ASTM D6110-04*; Standard Test Methods for Determining the Charpy Impact Resistance of Notched Specimens of Plastics. American Society for Testing and Materials (ASTM International): West Conshohocken, PA, USA, 2017.

66. *ASTM E384-17*; Standard Test Method for Microindentation Hardness of Materials. American Society for Testing and Materials (ASTM International): West Conshohocken, PA, USA, 2022.

67. *ASTM D1238-13*; Standard Test Method for Melt Flow Rates of Thermoplastics by Extrusion Plastometer. American Society for Testing and Materials (ASTM International): West Conshohocken, PA, USA, 2020.

68. Zimmerer, C.; Matulaitiene, I.; Niaura, G.; Reuter, U.; Janke, A.; Boldt, R.; Sablinskas, V.; Steiner, G. Nondestructive Characterization of the Polycarbonate–Octadecylamine Interface by Surface Enhanced Raman Spectroscopy. *Polym. Test.* **2019**, *73*, 152–158. [CrossRef]

69. Resta, V.; Quarta, G.; Lomascolo, M.; Maruccio, L.; Calcagnile, L. Raman and Photoluminescence Spectroscopy of Polycarbonate Matrices Irradiated with Different Energy 28Si+ Ions. *Vacuum* **2015**, *116*, 82–89. [CrossRef]

70. Bichara, L.C.; Alvarez, P.E.; Fiori Bimbi, M.V.; Vaca, H.; Gervasi, C.; Brandán, S.A. Structural and Spectroscopic Study of a Pectin Isolated from Citrus Peel by Using FTIR and FT-Raman Spectra and DFT Calculations. *Infrared Phys. Technol.* **2016**, *76*, 315–327. [CrossRef]

71. Synytsya, A. Fourier Transform Raman and Infrared Spectroscopy of Pectins. *Carbohydr. Polym.* **2003**, *54*, 97–106. [CrossRef]

72. Makarem, M.; Lee, C.M.; Kafle, K.; Huang, S.; Chae, I.; Yang, H.; Kubicki, J.D.; Kim, S.H. Probing Cellulose Structures with Vibrational Spectroscopy. *Cellulose* **2019**, *26*, 35–79. [CrossRef]

73. Stuart, B.H. Temperature Studies of Polycarbonate Using Fourier Transform Raman Spectroscopy. *Polym. Bull.* **1996**, *36*, 341–346. [CrossRef]

74. Lin, Z.; Guo, X.; He, Z.; Liang, X.; Wang, M.; Jin, G. Thermal Degradation Kinetics Study of Molten Polylactide Based on Raman Spectroscopy. *Polym. Eng. Sci.* **2021**, *61*, 201–210. [CrossRef]

75. Badr, Y.A.; Abd El-Kader, K.M.; Khafagy, R.M. Raman Spectroscopic Study of CdS, PVA Composite Films. *J. Appl. Polym. Sci.* **2004**, *92*, 1984–1992. [CrossRef]

76. Liu, X.; Zou, Y.; Li, W.; Cao, G.; Chen, W. Kinetics of Thermo-Oxidative and Thermal Degradation of Poly(d,l-Lactide) (PDLLA) at Processing Temperature. *Polym. Degrad. Stab.* **2006**, *91*, 3259–3265. [CrossRef]

77. Veselý, P.; Froš, D.; Hudec, T.; Sedláček, J.; Ctibor, P.; Dušek, K. Dielectric Spectroscopy of PETG/TiO$_2$ Composite Intended for 3D Printing. *Virtual Phys. Prototyp.* **2023**, *18*, e2170253. [CrossRef]

78. Dhotel, A.; Rijal, B.; Delbreilh, L.; Dargent, E.; Saiter, A. Combining Flash DSC, DSC and Broadband Dielectric Spectroscopy to Determine Fragility. *J. Therm. Anal. Calorim.* **2015**, *121*, 453–461. [CrossRef]

79. Song, Y.; Zheng, Q. Concepts and Conflicts in Nanoparticles Reinforcement to Polymers beyond Hydrodynamics. *Prog. Mater. Sci.* **2016**, *84*, 1–58. [CrossRef]

80. Zhang, H.; Zhu, H.; Xu, C.; Li, Y.; Liu, Q.; Wang, S.; Yan, S. Effect of Nanoparticle Size on the Mechanical Properties of Polymer Nanocomposites. *Polymer* **2022**, *252*, 124944. [CrossRef]

81. Chang, A.; Babhadiashar, N.; Barrett-Catton, E.; Asuri, P. Role of Nanoparticle–Polymer Interactions on the Development of Double-Network Hydrogel Nanocomposites with High Mechanical Strength. *Polymers* **2020**, *12*, 470. [CrossRef]

82. Zare, Y.; Rhee, K.Y.; Hui, D. Influences of Nanoparticles Aggregation/Agglomeration on the Interfacial/Interphase and Tensile Properties of Nanocomposites. *Compos. B Eng.* **2017**, *122*, 41–46. [CrossRef]

83. Liao, Y.; Liu, C.; Coppola, B.; Barra, G.; Di Maio, L.; Incarnato, L.; Lafdi, K. Effect of Porosity and Crystallinity on 3D Printed PLA Properties. *Polymers* **2019**, *11*, 1487. [CrossRef] [PubMed]

84. Wang, X.; Zhao, L.; Fuh, J.Y.H.; Lee, H.P. Effect of Porosity on Mechanical Properties of 3D Printed Polymers: Experiments and Micromechanical Modeling Based on X-Ray Computed Tomography Analysis. *Polymers* **2019**, *11*, 1154. [CrossRef] [PubMed]

85. Xu, G.C.; Wang, J.; Ji, X.L.; Xiong, J.Y.; Li, F. Effect of Nano-Silicon Nitride on the Mechanical and Electric Properties of Polypropylene Nanocomposite. *J. Compos. Mater.* **2007**, *41*, 2213–2223. [CrossRef]

86. Khan, M.I.; Umair, M.; Nawab, Y. 8—Use of Auxetic Material for Impact/Ballistic Applications. In *Composite Solutions for Ballistics*; Nawab, Y., Sapuan, S.M., Shaker, K., Eds.; Woodhead Publishing: Thorston, UK, 2021; pp. 199–228, ISBN 978-0-12-821984-3.